Summer 2016

A study on non-metallic inclusions in foundry steel process

Marc Leonard Harris

Department:

A STUDY ON NON-METALLIC INCLUSIONS IN FOUNDRY STEEL PROCESS

by

MARC LEONARD HARRIS

A THESIS

Presented to the Faculty of the Graduate School of the

MISSOURI UNIVERSITY OF SCIENCE AND TECHNOLOGY

In Partial Fulfillment of the Requirements for the Degree

MASTER OF SCIENCE IN METALLURGICAL ENGINEERING

2016

Approved by

Von L. Richards, Advisor
Simon Lekakh
Ronald O'Malley

PUBLICATION THESIS OPTION

This thesis has been prepared in the form of three manuscripts for publication. Paper I, pages 5–21, was published May 2015 in AISTech, 2015. Paper II, pages 22–39, will be submitted for publication in the International Journal of Metals Casting. Paper III, pages 40–56, will be submitted for publication in the International Journal of Metals Casting. The Introduction and Appendices provide supplemental information to certain experimental procedures and calculations.

ABSTRACT

The effects of sample area and automated SEM/EDS feature analysis parameters (step size, magnification and threshold) on nonmetallic inclusion characterization results has been investigated and optimized. A post-processing program was developed to automatically determine average inclusion chemistry, total element concentrations within inclusions, and for generating joint ternary diagrams with size visualization for representing nonmetallic inclusion populations. Using these tools the evolution of nonmetallic inclusions was examined for 4320 steel at a participating industrial steel foundry. The steel was sampled throughout electric arc furnace melting through ladle refining to the final casting where an in-mold sampling procedure was developed to procure numerous test samples representative of final heavy section castings in effort to further understand the effect of different metallurgical factors on impact toughness for slow solidification rate high strength cast steel. Nonmetallic inclusion nucleation, growth, and flotation were monitored through liquid steel processing by size-classified area fraction. The use of zirconium as an addition for nitrogen/oxygen removal was found to lead to a large number of ZrO_2 inclusions, which resulted in insufficient flotation due to the higher density of zirconia and, less effective calcium treatment. No ZrN formation was observed owing to the high FeO acid slag practice used. Argon stirring was found to mitigate the flotation problems associated with the zirconium addition and significantly contribute to the removal of large size (>5μm) inclusions. In-mold heavy section samples were tested at -40°C and 25°C to examine how different microstructural features such as nonmetallic inclusions, porosity, and hardness influence the impact energy of the steel for brittle and ductile fracture modes. SEM fractography was used to characterize failures modes: brittle, ductile, and quasi-ductile at energies ranging from 14-40 ft-lbs. For brittle fracture, hardness had an adverse influence on impact energy absorbed, while increasing the average area fraction and diameter of nonmetallic inclusions led to improved toughness. The opposite trends were observed for ductile fracture in specimens tested at room temperature, where area fraction of nonmetallic inclusions and porosity were detrimental to the impact energy absorbed.

ACKNOWLEDGMENTS

It has been an honor to work with Dr. Von Richards on this project and I would like to give thanks for all the exceptional guidance, knowledge, and dedication he provided. I would also like to thank Dr. Simon Lekakh for the countless ideas and aid in experimentation. Many thanks to Dr. Ronald O'Malley who has consistently given reliable guidance throughout the course of this research. Additionally, I would like to express my gratitude to all of the undergraduate and graduate students who helped with this work: Zach Henderson, Daniella Bahiense-De Oliviera, Zachary Hilton, Chris Ferris, Tim Adams, Elaina Hodges, Sean Duran, Rairu Penna, Mingzhi Xu, Jingjing Qing, Obinna Adaba, Andrew Russo, Daniel Field, and Terrell Webb. I would also like to thank the Peaslee Steel Manufacturing Research Center for its financial support and the associated industrial committee for its guidance throughout the project. I am also appreciative of the Foundry Educational Foundation for their financial support in awarding me the H.H. Harris scholarship.

TABLE OF CONTENTS

LIST OF ILLUSTRATIONS

PAPER II

PAPER III

LIST OF TABLES

1. INTRODUCTION

1.1 AUTOMATED SEM/EDS SYSTEM

There is a growing need for time efficient, effective methods of characterizing vast numbers of inclusions for the modern day steel producers. Although there are a vast number of techniques available for characterization of inclusions, automated SEM/EDS systems often fill this role providing the means to rapidly characterize thousands of nonmetallic inclusions in a few hours while providing information about size, chemical composition, and positions [1-12]. These have become popular among steel mills and have proven applicable to steel foundries but procedures will differ greatly as there are large differences in process and cleanliness requirements. Care must be taken in data collection and any conclusions drawn from such a highly automated system. Often, small polished sections from samples taken during liquid steel processing are analyzed and represent only a small fraction of the melt volume but are treated as representative. In addition, the collected liquid steel in the sampler is subjected to different cooling rates during solidification that can alter the inclusion characteristics[13,14]. Ruby-Meyer et al performed CFD Fluent calculations that showed the last section to solidify in an immersion sampler is at the center[5]. Ola Ericsson investigated the solidification rate for a 12 mm thick stainless steel immersion sample and discovered that solidification rates could differ by as much as 10 °C/s [9]. In addition to sample representativeness, the automated SEM/EDS system settings and the methods used to post process the acquired data can also lead to misinterpretations [11].

A methodology has been developed that allows for accurate, repeatable inclusion analysis using an automated feature analysis SEM/EDS system. This was done using the ASPEX Pica 1020 SEM/EDS system, the basic functionality of which was examined. Industrial steel foundry samples were collected from liquid processing steps with the aim of developing repeatable methods of in-depth nonmetallic inclusion analysis.

1.2 NUCLEATION, GROWTH, & FLOTATION

Nonmetallic inclusions can be formed as a result of solubility limits in classic nucleation theory (indigenous), or be a result of some external contamination event

(exogenous). The most common source of nonmetallic inclusions is from reactions with dissolved active elements such as oxygen, nitrogen, or carbon forming oxides, nitrides, and carbides respectively. Typically for steel castings, porosity is considered highly undesirable and the most common method to eliminate gas (CO) formation upon solidification is the use of deoxidizers (usually aluminum or silicon). This is an effective method of deoxidation but results in the generation of a numerous oxide population. These oxides can be highly problematic for certain steel grades with stringent specifications and can have negative effects on castability, mechanical properties, or even complying with cleanliness requirements[14-22].

The current understanding of the evolution of nonmetallic inclusions is composed of three stages: (i) nucleation, (ii) growth/agglomeration, and (iii) flotation[14,15]. Nucleation is largely understood as competing reactions of surface energy minimization and bulk free energy minimization such that above some critical radius a nucleus is successfully formed and spontaneously grows. Growth of a nonmetallic inclusion can occur through a variety of mechanisms driven by diffusion, local thermodynamics, Ostwald ripening, or physical agglomeration. For sub-micron sized inclusions, agglomeration is thought to be the result of Brownian collision whereas larger inclusions are more affected by macroscopic melt flow and can be greatly influenced by differential flotation velocities in accordance with Stoke's Law[14,15]. This agglomeration process can be made more efficient if the inclusions are in a liquid state which is one goal of CaSi modification of Al_2O_3. The calcium in this case leads to the formation of a $CaO{\cdot}Al_2O_3$ liquid state inclusion that is both spherical and has increased tendency to agglomerate to other solid Al_2O_3 inclusions which increases flotation velocity by increasing the radius[14-18].

Shown below is Stokes' Law for unstirred systems with low Reynolds numbers where the velocity of a particle is dependent on the density differential and its size according to Equation 1:

$$v_s = \frac{2(\rho_p - \rho_f)}{9\mu} g R^2 \qquad (1)$$

where: v_s is the particle velocity, ρ_p is the particle density, ρ_f is the fluid density, g is the gravitational constant, and R is the particle radius. Stirring increases net flotation by both

increasing overall fluid velocity, and through inclusion wetting and attachment to the bubble itself. The gas used is typically argon and enters through an eccentrically located porous plug in the ladle bottom[23]. Reynolds numbers for stirred cases are typically too large for Stokes' Law to be the dominant flotation mechanism, rather than macroscopic flow.

Recent work on the evolution of inclusions in continuous casting steelmaking processes has employed automated SEM-EDS systems [1-4,6,7,24]. When attempting to apply a similar approach for industrial foundry settings it is important to remember the formation of inclusions in a steel mill can be more controlled with limited oxygen exposure, narrow ranges of alloying, and consistent product geometry and size. These types of restrictions are often infeasible for foundries where castings are complex and variable. Work by Singh et al. examined the effectiveness of calcium treatments on the nonmetallic inclusion population while discussing optimum treatments by using an automated SEM/EDS[6,7]. Here a similar approach was used to evaluate the deoxidation practice, calcium treatment effectiveness, and the effect of argon stirring in an effort to understand the overall evolution of inclusions in the steel foundry processing route for carbon and low alloy steel castings.

1.3 MECHANICAL PROPERTY RELATIONSHIPS

Several microstructural parameters (nonmetallic inclusions, porosity, microstructure and hardness) are critical in terms of mechanical properties, especially impact properties of steel. The number density of inclusions, the volume fraction, and the average spacing of the inclusions have been shown to have a strong correlation with impact energy absorbed at room temperature[25-30]. Increasing volume fraction and number density have been found to negatively impact the dynamic fracture toughness while a smaller inclusion spacing lowers the energy absorbed[25]. The previous work relating these variables has been done at room temperature (25°C) where ductile fracture is the predominant fracture mode for the steels considered; however, the majority of the studies performed impact tests using specially rolled or cast specimens that did not necessarily reflect the properties actual heavy section castings[25-30].

Studies from Peaslee et al. and Bartlett et al. have used automated SEM/EDS systems for nonmetallic inclusion analysis for impact test analysis[24,25]. The large number of inclusions analyzed via automated SEM/EDS in these studies has allowed more repeatable and statistically significant information to be gathered about the behavior of ductile fracture in the presence of nonmetallic inclusions. This work will expand on the earlier observed relationships considering the effects of different microstructural features in heavy section castings on absorbed impact energy for different fracture modes. Samples were tested at -40°C and 25°C with the goal of linking characteristics of nonmetallic inclusions, porosity, and hardness to impact toughness while keeping the fracture mode consistent for each test temperature. Fracture modes are of course related to the heat treatment process and specifically the microstructure of the steel[30]. Effort was done to collect specimens for testing directly in the mold, which represent the real heavy section castings without the necessity of destroying the final product.

PAPER

I. Improved Methodology for Automated SEM/EDS Non-Metallic Inclusion Analysis of Mini-Mill and Foundry Steels

Marc L. Harris, Obinna Adaba, Von L. Richards, Simon Lekakh, Ronald O'Malley

Metallurgical Engineering
Missouri University of Science and Technology
223 McNutt Hall, 1400 N. Bishop, Rolla, MO 65409-0330, USA
Tel.: 573-341-4717
Email: vonlr@mst.edu

Abstract

Automated Feature Analysis (AFA) provides the means to rapidly characterize large inclusion populations. System settings must be optimized to properly detect and interpret the important inclusion characteristics. The effects of sample area and AFA parameter settings (step size, magnification and threshold) on inclusion characterization results has been investigated and optimized. Methodologies for determining average inclusion chemistry, total element concentrations within inclusions, and for using joint ternary diagrams with size visualization to represent inclusion populations are presented. These methodologies were applied to samples collected from industrial steel mill and steel foundries and demonstrated in this study.

Introduction

Non-metallic inclusions are an inevitable consequence of steelmaking and are undesirable for the most part. Mechanical properties are largely affected by them and some inclusions promote clogging of submerged entry nozzles (SEN) [1-4]. Complete removal however is not necessary and cleanliness requirements are determined by various thresholds on inclusion characteristics such as amount, size, composition, and distribution[1,5]. These

thresholds vary by grade and requirements are increasingly more stringent. Much research has been conducted on methods of inclusion control to minimize the potentially detrimental effects on final properties and there are a vast number of techniques available for characterization of inclusions[1-12]. There is however, a growing need for a time efficient, effective method of characterizing vast numbers of inclusions for the modern day steel producers.

Automated SEM/EDS provides the means to rapidly characterize large inclusion populations providing information about amount size, composition and distribution of inclusions. With the growing computational power available, post-processing of the vast quantities of data output by such a system has also become more efficient. These devices have become popular among steel mills and have proven to be applicable to steel foundries, although, procedures will differ greatly owing to the large difference in process and cleanliness requirements. Precautions also need to be taken in data collection and analysis. Small polished sections from samples taken during liquid steel processing are analyzed and represent only a small fraction of the melt volume while typically being assumed as representative. In addition, collected liquid steel in the sampler is subject to different cooling rates during solidification that can alter the inclusion characteristics[13-14]. Ruby-Meyer et al [5]showed using CFD Fluent calculations that the last section to solidify in a lollipop sampler is at the center. Ola Ericsson[9] investigated the solidification rate for a 12 mm thick stainless steel lollipop sample and observed that the solidification rate could differ by as much as 10 °C/s. System parameter settings and the methods used to post process the typically large quantity of data obtained in an SEM/EDS scan can also lead to misinterpretations.

A methodology has been developed and presented here for accurate, repeatable inclusion analysis using an automated feature analysis SEM/EDS system. This is based on experiments conducted at the Peaslee Steel Manufacturing Research Center (PSMRC), Missouri University of Science and Technology. The ASPEX Pica 1020 SEM/EDS system was used in this study, the basic functionality of which was examined. Both

foundry and mill samples were collected from liquid processing steps with the aim of developing accurate and repeatable methods of in-depth inclusion analysis.

Experimental Procedure

Sample Collection & Preparation. Industrial samples were taken during liquid steel processing using un-killed sampler types in order to prevent non-representative inclusion populations from forming. Steel chilled immersion samplers were chosen for their wide applicability and common use in industry. For this reason both center and surface sections were considered for analysis: representing different cooling rates in the sampler. Figure 1 is a schematic of both section locations in the sampler. Grinding was done using SiC media (180, 400, 600, 1200 grits), polished using 3µm diamond paste, and finished using a 0.1µm diamond paste. Metallographic preparation was done in accordance to ASTM E3-11 for all samples.

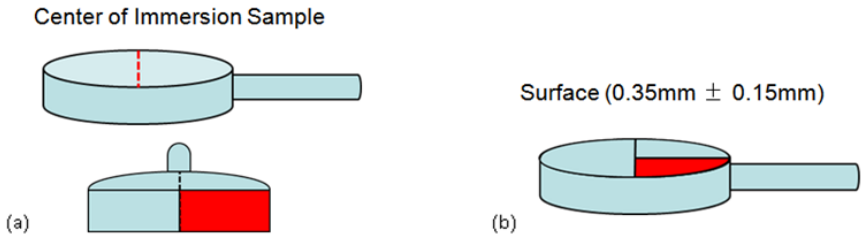

Figure 1. Schematic of immersion samplers with a) center sectioning region highlighted and b) surface sectioned area highlighted (approximately 0.35 mm below surface after sample grinding and polishing).

Automated SEM/EDS Analysis. After preparation, samples were scanned using an automated SEM/EDS system (ASPEX PICA 1020), the simplified procedure of which can be broken down into four steps: 1) SEM location of a feature of high z-contrast; 2) EDS spectrum analysis of the located high z-contrast feature; 3) check of spectrum counts to exclude porosity; 4) recording of all relevant data. Consideration of only a limited number of elements aided in minimizing error in compositional data obtained from EDS spectra. Elements considered included: Mg, Al, Si, Zr, S, Ca, Ti, and Mn. Fe

was not considered in the EDS spectra as the interaction volume of the electron beam would affect compositional results in favor of Fe. Scans were performed with varied minimum diameter thresholds, step sizes, and magnification and the effect of these parameters on detection capabilities considered. Approximately 15-30% dead time was used, 20 kV accelerating voltage, and a nominal EDS detection time of 1 second (optimal settings for the instrument and elements of interest). Porosity was excluded from consideration using an EDS count threshold of 1000, an example of which can be seen in Figure 2. A Monte-Carlo simulation of randomly distributed inclusions showed that 500-700 counted inclusions from each specimen is enough to accurately represent the inclusion population. In this study, an average of 2500 inclusions were experimentally counted for improved statistical analysis

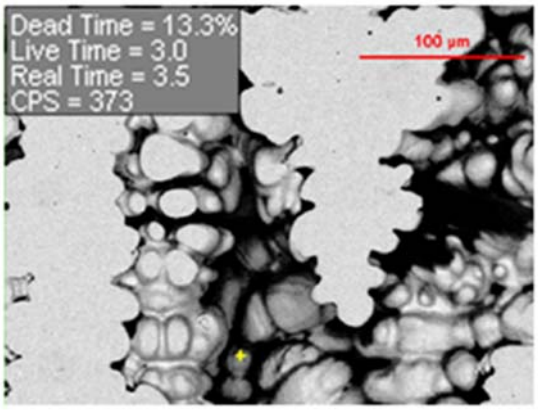

Figure 2. Large region of porosity with low counts per second (CPS) that leads to exclusion from analysis.

Results

ASPEX Settings. Figure 3 is a schematic of how detection and measurement is done using the ASPEX. The electron beam moves in steps (bold black dots) which are determined by the SEM step size setting used. Once a feature is detected a much finer resolution is used (smaller dots) for the measurement of the inclusion. With increasing step size, the possibility of detecting small features decreases, and as the magnification increases, the separation of the smaller dots decreases thus, increasing the accuracy of

measurement. Before the start of an AFA, a minimum diameter threshold is set that determines the minimum size of an inclusion that will be characterized. It is therefore important that the selected step size is less than the minimum diameter threshold setting to detect the maximum number of inclusions.

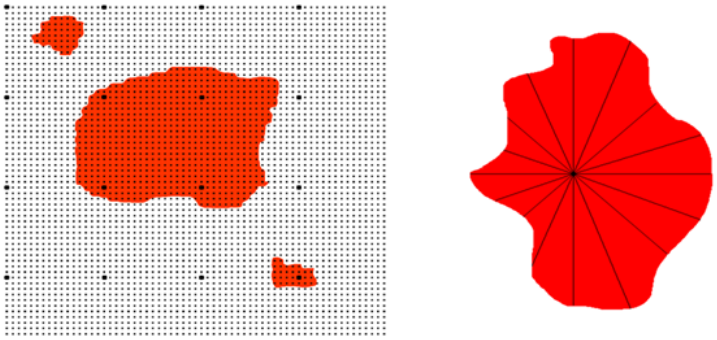

Figure 3. ASPEX feature detection method and area measurement methods.

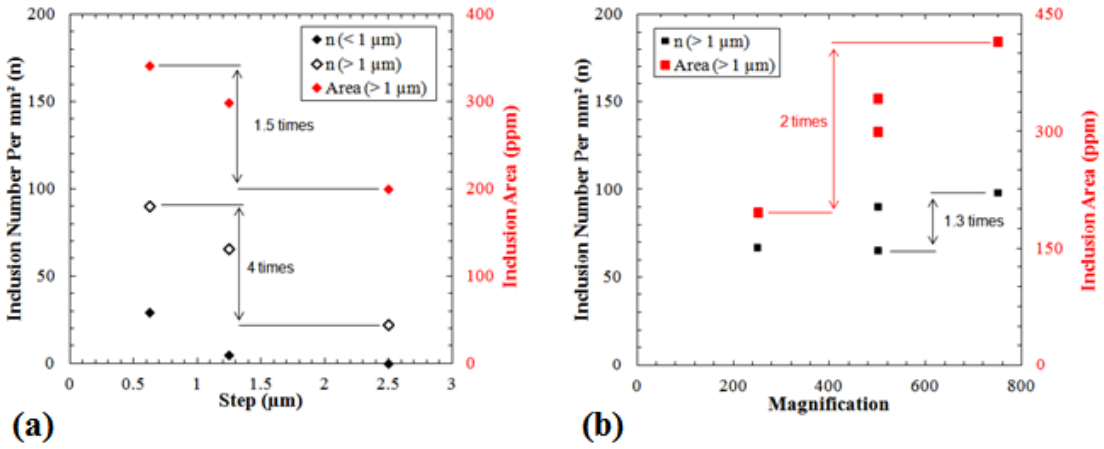

Figure 4. Effect of (a) step size and (b) magnification on number of inclusions detected per area and inclusion area fraction.

Figure 4 shows how the experimentally measured number density and area fraction vary with both step size and magnification for the same analyzed area. The counted values of both number density and area fraction decrease with increasing step size and increase with increasing magnification. Step size was found to have a larger effect on number density while area fraction is affected more by the magnification.

The analyzed area fraction and number of detected inclusions was found to be heavily dependent on the minimum diameter threshold chosen (see Figure 5). The behavior of this curve suggests that a minimum diameter threshold of approximately 0.75 µm should be the largest chosen for an encompassing analysis. As the threshold increases beyond 0.75 µm the resulting area fraction and number of detected inclusions drops significantly, as large numbers of inclusions are going undetected. The variation of the number of detected inclusions below 0.75 µm is reduced but still increases continuously, evidence that there is a population of sub micron (< 0.5 µm) sized inclusions that were not detected. The minimum diameter threshold could not be reduced below 0.5 µm as it was the limit of accurate detection of the instrument; however the area fraction contribution of such small inclusions was determined to be insignificant. Below 0.75 µm in diameter the variation for the resulting area fraction is minimal indicating the true value of the sample area fraction has been obtained since detection of smaller inclusions has no observable effect.

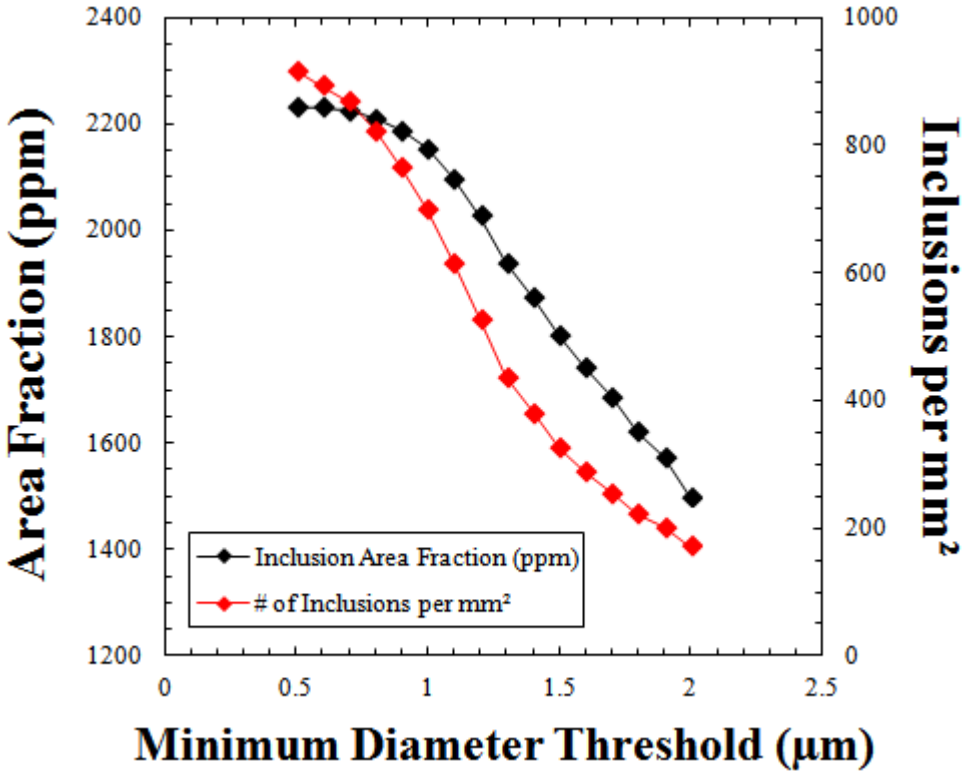

Figure 5. Effect of minimum size setting on reported area fraction and population density.

It was found that scans performed using a 0.5 μm minimum diameter threshold (limit of instrument) were optimal for determining an accurate inclusion area fraction. A search grid step size of 0.16 μm was determined to be more than sufficient for 100% detection of inclusions as small as 0.5 μm in diameter (≤0.35 μm according to Equation 1). The optimal step size is related to the minimum diameter threshold as:

$$s \leq \frac{\sqrt{2}}{2} D_{min} \qquad (1)$$

where: s is the search grid step size, and D_{min} is the minimum diameter threshold. This relationship holds for a square search grid pattern and is based on the worst case scenario of an infinitesimally thin inclusion extending from one corner of the search grid to the other. The result is the maximum step size for 100% detection of inclusions as small as D_{min}.

To further understand the effect of settings on the measured number density and area fraction of inclusions a test was carried out using the SEM calibration standard (Figure 6). The standard is composed of different sized spherical particles and Figure 7 shows the change in measured aspect ratio and size of the detected features for different magnifications. It can be seen that as the magnification increases the measured aspect ratio decreases and the diameters approach the actual values (1, 2, 3..10 μm). Additionally, the variation in both aspect ratio and the diameter from the known value decreases. This is due to increased accuracy of measurement, as a larger pixel density from high magnification gives more accurate measures of area, diameter, and aspect ratio.

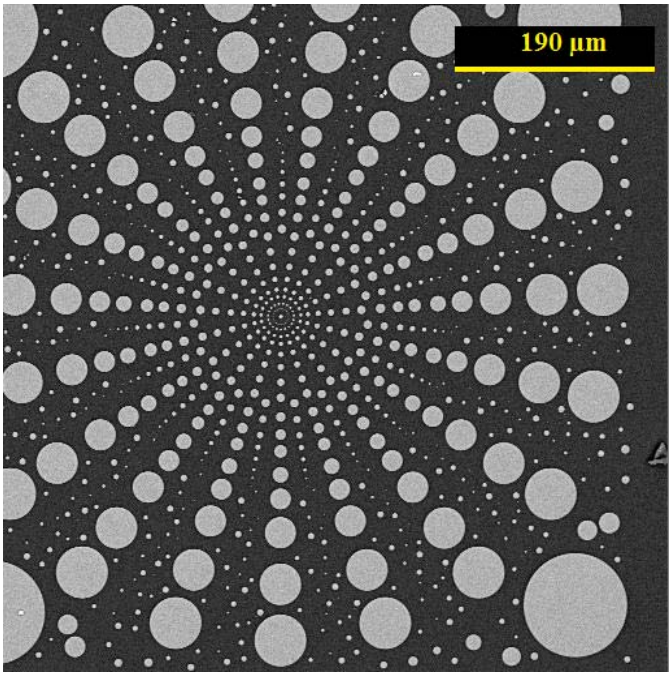

Figure 6. SEM image of calibration standard with known size distribution and aspect ratio of 1.

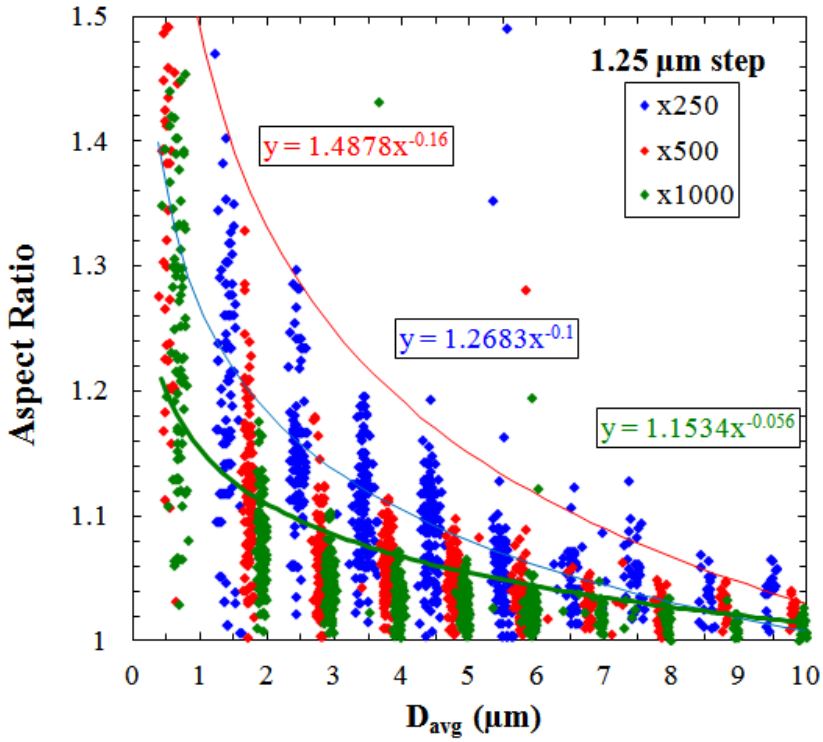

Figure 7. Effect of magnification on the measured particle size and aspect ratio.

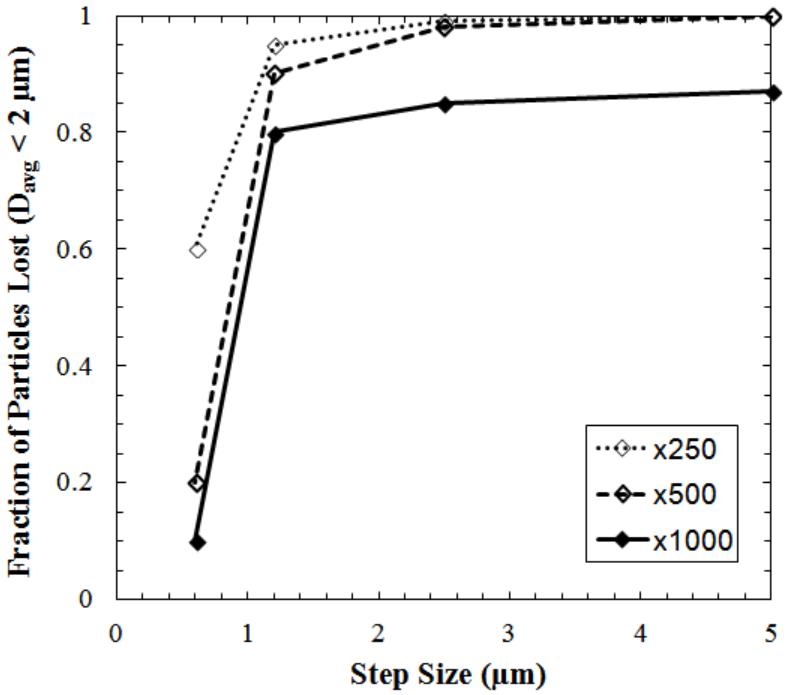

Figure 8. Fraction of undetected small particles below 2 µm diameter for varied step sizes and magnification where 0 denotes no missed particles and 1 denotes total loss.

A quantitative example of the effect of step size and magnification on the fraction of detected particles can be seen most prominently in Figure 8. For small sized inclusions the larger step sizes result in no detection (>80% loss), and for magnifications that are too low the same occurs (differences of 20-50% in detection).

Mass Balance Calculations. A method of calculating a mass balance from SEM-EDS data was developed that allows the study of elemental content contained within inclusions. The areal average elemental composition of inclusions is calculated for each element as follows:

$$\%m = \frac{\sum(\%x)(A_{inclusion})}{A_{total}} \qquad (2)$$

where: *%m* is the areal average mass percent of a given element, *%x* is the amount of respective element in an individual inclusion, $A_{inclusion}$ is the area of the individual inclusion, and A_{total} is the total area of all measured inclusions. The mass balance calculation was performed using the compositional data obtained from the SEM-EDS inclusion analysis and Equation 3:

$$M_{ppm} = \frac{\%m\, A_f\, \rho_i\, w_i}{100\rho_m} \quad (3)$$

where: M_{ppm} is the mass fraction in ppm of a given element in a sample contained within inclusions, $\%m$ is the areal average mass percent of a given element, A_f is the total inclusion area fraction, ρ_i is the density of the inclusion associated with the given element, ρ_m is the density of the matrix (taken to be iron), and w_i is the mass fraction of the given element in the associated inclusion compound.

The results of these mass balance calculations were extended to calculate the approximate amount of total oxygen in the samples through the assumption of most-stable compound. This was done as a means to meter the accuracy of the mass balance calculations as oxygen is a low solubility element in iron, almost entirely present in the steel in the form of oxide inclusions. In order to calculate the oxygen content, sulfides were filtered via a sulfur threshold and the remaining inclusions assumed to be stable oxides with the appropriate stoichiometry. The accuracy of varied sulfide thresholds on the total oxygen calculation was compared to an inert gas fusion analysis of total oxygen (see Figure 9). A 30% threshold of sulfur was found to be in closest agreement with the inert gas fusion analysis results. A direct comparison of total oxygen is shown in Figure 10 as a function of process time for two industrial trials. The accuracy of the calculated results is close or inside the 95% confidence interval for most of the inert gas fusion analysis method results and is consistent enough to represent the same trends, indicating the mass balance results are reasonable. Additionally the calculated results are largely within less than 50 ppm of the reported inert gas fusion results with few exceptions.

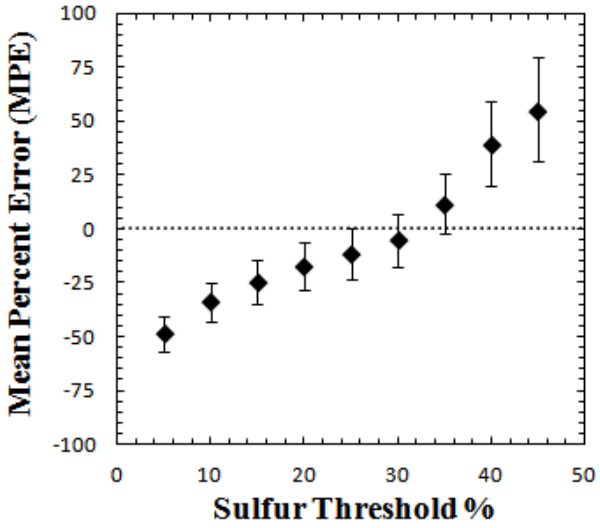

Figure 9. Mean percent error of calculated total oxygen from SEM/EDS data compared to inert gas fusion method versus sulfur threshold used in analysis.

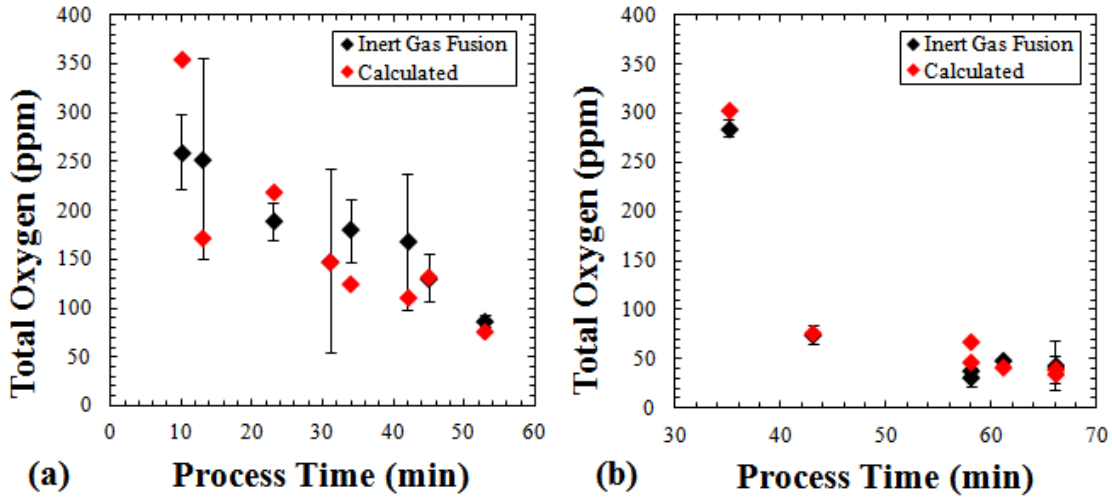

Figure 10. Total oxygen content measured by two methods (calculated with a 30% sulfur threshold and inert gas fusion) in samples taken throughout liquid processing at a) Foundry A and b) Foundry B.

The optimal sulfur threshold was applied in a mass balance calculation of manganese rich inclusions and the results can be seen in Figure 11 for both unfiltered and only oxide inclusions. This method allows examination of mass quantities associated with specific inclusion populations, in this case manganese oxide.

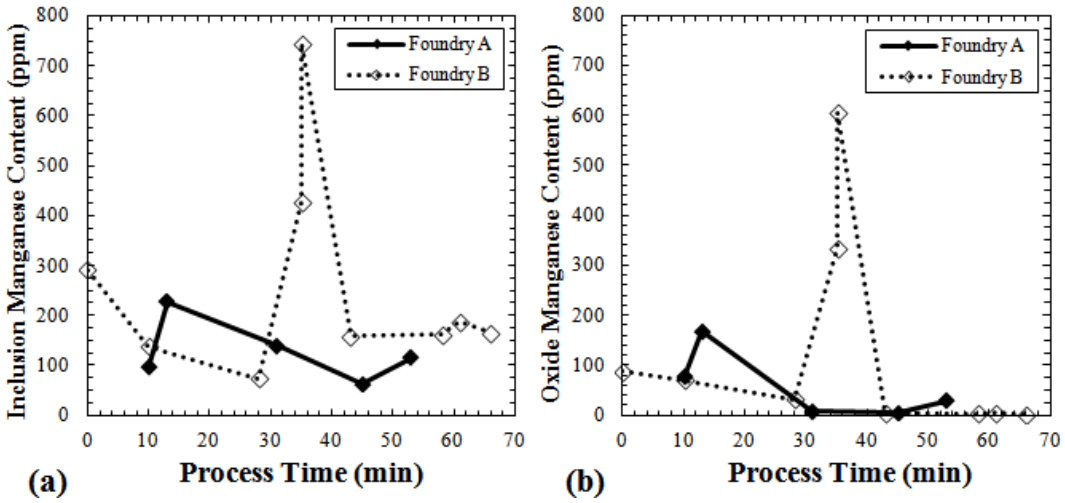

Figure 11. Manganese content within a) all inclusions scanned and b) only oxides < 30% sulfur.

Analyzed Section Area. Comparing the results for the two sectioning methods, it was found that the center sectioned immersion samples had a larger measured inclusion area fraction than the surface method (see Figure 12). This has been attributed in large part to inclusions formed at low temperatures such as manganese sulfide, which depend largely on cooling rate. The surface ground region of the immersion sample is the closest to steel chill plates resulting in much faster cooling rates compared to the central region of the sample. That is, the slower cooling rate in the center allows more time for inclusions such as manganese sulfide to form while the faster cooled surface does not. Inclusions such as manganese sulfide, which form during solidification or upon cooling, can alter primary inclusions: those that are present in the liquid steel. These primary inclusions often serve as sites for preferential nucleation which affects the measured composition and size. It is important that areas selected for analysis be representative of primary inclusions when trying to study liquid steel processing. Thus, the most representative section of the immersion sampler is the surface (fastest cooling) but is also the most prone to contamination via slag entrainment and flotation effects. In some cases center sectioning is a superior alternative, especially when contamination issues are prevalent.

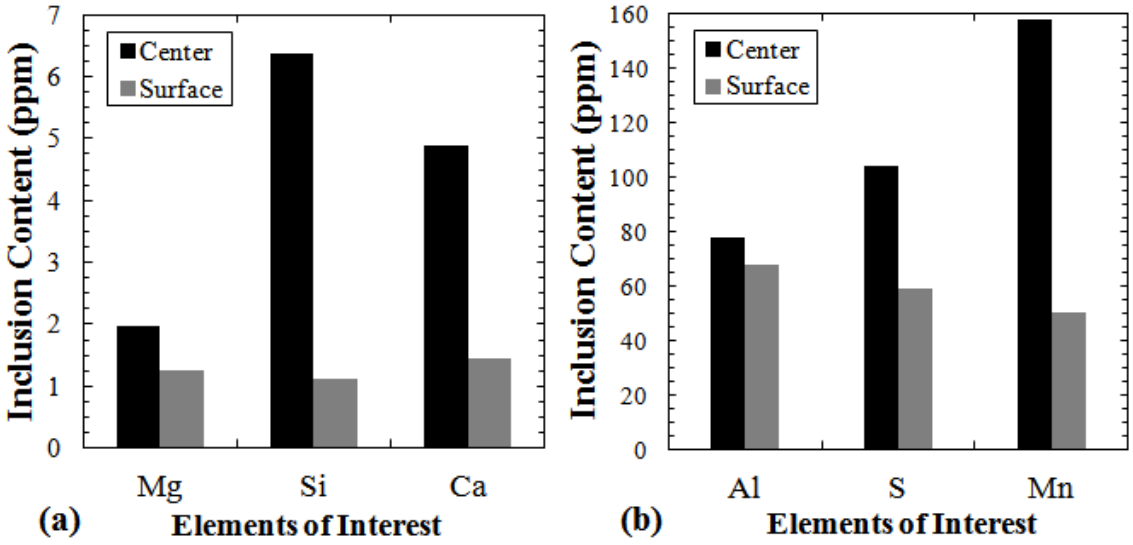

Figure 12. Elemental content within all scanned inclusions in specimens prepared by two sectioning methods: a) minor elements and b) major elements present in inclusions.

Discussion

Inclusion compositions are typically represented using single ternary diagrams. The problem with this form of representation is that the inclusion populations present contain more than three elements (often 6 or 7 depending on the composition of the steel). Normalization is therefore implicit in these representations and can lead to large errors in interpretation. A system was developed for representing different inclusion classes by combining six different ternaries allowing for the representation of up to 7 elements. Each ternary represents a distinct inclusion population with each individual inclusion counted only once and shown in the respective ternary section it belongs. The technique considers the three most abundant elements of a particular inclusion in assigning ternary sections and these elements typically account for more than 80% of the inclusion composition, thus errors associated with normalization are greatly reduced. In addition to minimizing normalization errors, ternaries seldom have morphological factors such as size included which can mislead interpretation (e.g. large exogenous inclusions of differing composition). Therefore, inclusion diameter is also represented in the joint ternaries developed in this study and displayed through different colors and marker size.

Figure 13 is an example of a joint ternary showing the advantage of this method of representation where different types of inclusions can be examined in a continuous plot.

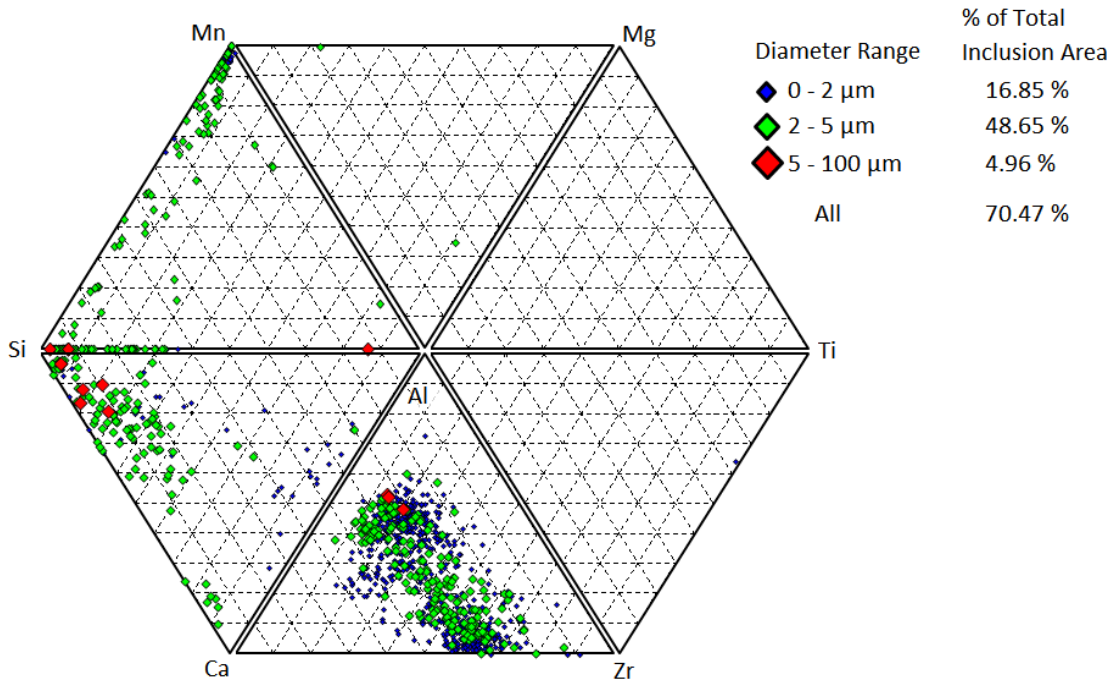

Figure 13. Joint ternary showing different classes of inclusions and their respective sizes (depicted through different colors and sizes of markers).

The evolution of inclusions throughout liquid processing has been studied for both foundry and mill samples using joint ternaries yielding a more comprehensive understanding of inclusion development. Figure 14 shows one such analysis for samples taken at different stages of LMF processing in a mini mill with the phase boundaries overlaid on the diagram. The heat studied was aluminum killed, calcium treated, and was the second heat of a four heat sequence. The ternaries shown represent samples taken after de-oxidation, before de-sulfurization, after de-sulfurization, and after calcium treatment. After de-oxidation, the inclusion population is seen to be aluminum rich (Figure 14a). With time, coarsening is observed in the aluminum oxide inclusion population (Figure 14b). After de-sulfurization there is a shift in the inclusion population towards spinel formation (Figure 14c). After calcium treatment, modification of alumina and spinel inclusions is observed as well as the formation of large calcium sulfide (CaS) population (Figure 14d).

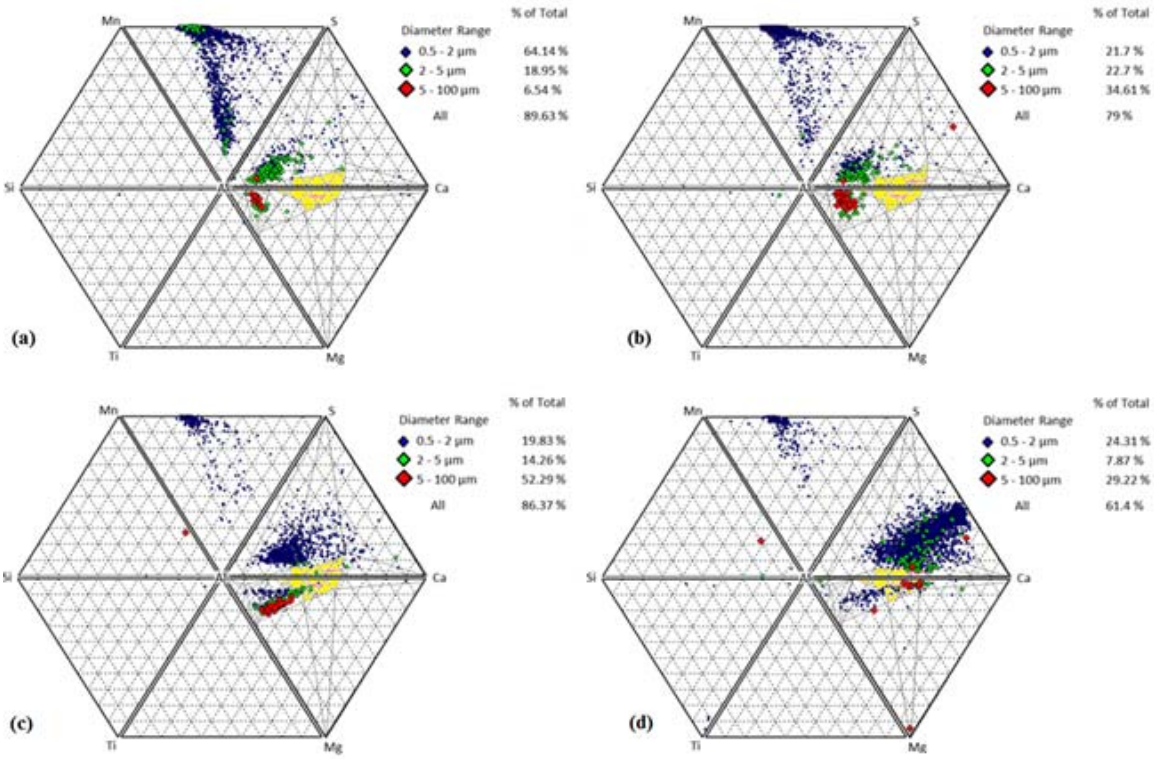

Figure 14. Joint ternaries for samples taken in a steel mini mill (a) after de-oxidation, (b) before de-sulfurization, (c) after de-sulfurization, and (d) after calcium treatment.

Conclusions

The effect of AFA settings: step size and magnification, on the number density and area fraction of inclusions was investigated using an automated SEM/EDS system along with sampling technique. Both the number density and area fraction increased with increasing magnification and decreased with increasing step size. The magnification was found to have a greater effect on the measured area fraction and diameter, while the step size had a more pronounced effect on the number of inclusions detected. For accurate analysis, the selected step size should be less than the minimum diameter threshold selected for inclusion analysis in accordance with Equation 3. It was also found that analysis of a rapidly cooled sample resulted in a more accurate representation of inclusion populations present in liquid steel; however the surface was found to be more likely to be contaminated with entrained slag.

New post processing methods and representation techniques for inclusion data acquired from SEM/EDS systems have been developed. These included: areal average compositions, mass balance calculations yielding the mass of an element in a sample present in the form of inclusions, and joint compositional ternaries with size data included. The mass balance correlation accuracy was measured through an oxygen result comparison with the more established inert gas fusion analysis technique and found to be largely within the 95% confidence intervals. This mass balance technique was used in the sample sectioning representativeness study. In addition to a mass balance calculation technique, a method of qualitatively displaying inclusion compositions and morphologies for highly varied inclusion populations was established as an expansion of more traditional single ternaries in the form of a joint ternary system.

References

1. Zhang, Lifeng, and Brian Thomas. "State of the Art in the Control of Inclusions during Steel Ingot Casting." *METALLURGICAL AND MATERIALS TRANSACTIONS B* 37B.October (2006): 733-60. Print.
2. Winkler, W., J. Angeli, and M. Mayr. "Automated SEM-EDX Cleanness Analysis and Its Application in Metallurgy." *BHM* 152.1 (2007): 4-9. Print.
3. Kaushik, P., H. Pielet, and H. Yin. "Inclusion Characterisation – Tool for Measurement of Steel Cleanliness and Process Control: Part 1." *Ironmaking and Steelmaking* 36.8 (2009): 561-71. Print.
4. Kaushik, P., H. Pielet, and H. Yin. "Inclusion Characterisation – Tool for Measurement of Steel Cleanliness and Process Control: Part 2." *Ironmaking and Steelmaking* 36.8 (2009): 572-82. Print.
5. Meyer F Ruby, Evrard S. Vergauwens M., Balland P. “Improvement of the Sampling Methodology for the Cleanliness Measurement in the Liquid Steel Stage.” *AISTech 2013 Proceedings* (2013): 1051-059. Print
6. Singh, Vintee, Kent Peaslee, and Simon Lekakh. "Use of Automated Inclusion Analysis to Evaluate the Effects of Ladle Treatment on Steel Cleanliness." 63rd SFSA T&O (2009): 1-15. Print.

7. Singh, Vintee, Simon Lekakh, Timothy Drake, and Kent Peaslee. "Process Design of Inclusion Modification in Cast Steel Using Automated Inclusion Analysis." *AISTech 2009 Proceedings* (2009): 1-11. Print.
8. Shi, Dexiang, and Douglas Winslow. "Accuracy of a Volume Fraction Measurement Using Areal Image Analysis." *Journal of Testing and Evaluation* (2012): 210-13. Print.
9. Ericsson, Ola. *An Experimental Study of Liquid Steel Sampling*. Thesis. Royal Institute of Technology, 2009. Print.
10. Nuspl, Markus, Wolfhard Wegscheider, Johann Angeli, Wilhelm Posch, and Michael Mayr. "Qualitative and Quantitative Determination of Micro-inclusions by Automated SEM/EDX Analysis." *Analytical and Bioanalytical Chemistry* 379 (2004): 640-45. Print.
11. Michelic, Susanne, Gerhard Wieser, and Christian Bernhard. "On the Representativeness of Automated SEM/EDS Analyses for Inclusion Characterisation with Special Regard to the Measured Sample Area." *ISIJ International* 51.5 (2011): 769-75. Print.
12. Abraham, Sunday, Justin Raines, and Rick Bodnar. "Development of an Inclusion Characterization Methodology for Improving Steel Product Cleanliness." *AISTech 2013 Proceedings* (2013): 1069-084. Print.
13. Zhang, Zhi, Anders Tilliander, Andrey Karasev, and Par Jonsson. "Simulation of the Steel Sampling Process." ISIJ International 50.12 (2010): 1746-755. Print.

II. Evolution of Non-Metallic Inclusions in Foundry Steel Casting Processes

Marc L. Harris, Von L. Richards, Simon Lekakh, Ronald O'Malley

Metallurgical Engineering
Missouri University of Science and Technology
223 McNutt Hall, 1400 N. Bishop, Rolla, MO 65409-0330, USA
Tel.: 573-341-4717
Email: vonlr@mst.edu

Abstract

The evolution of nonmetallic inclusions was examined for 4320 steel at an industrial steel foundry. The steel was followed from electric arc furnace melting through ladle refining to final casting. Timed sampling was performed at all stages of the process. Samples were analyzed using an automated SEM/EDS system. The overall evolution of oxide inclusions in terms of nucleation, growth, and flotation during liquid processing was studied using area fraction and average diameter. Chemical composition evolution was observed using a joint ternary plotting tool developed under this program. It was found that the use of zirconium as an addition for nitrogen/oxygen removal leads to a large number of ZrO_2 inclusions, which is related to insufficient flotation due to the higher density of zirconia and in turn less effective calcium treatment. In addition, no ZrN formation was observed, likely due to the high FeO acid slag practice used. Argon stirring was found to reduce the flotation problems associated with the zirconium addition somewhat and significantly contribute to the removal of large size (>5μm) inclusions.

Introduction

Steel cleanliness is of increasing interest as demand increases for high quality, clean steel castings. Mechanical properties are affected by inclusion size, number, and morphology. Therefore research is being conducted to improve inclusion control thus minimizing the detrimental effects of inclusions on final properties. The evolution of nonmetallic

inclusions throughout the production process must first be understood and controlled in order to control the final inclusion population.

Nonmetallic inclusions can be formed in the melt and upon solidification (indigenous) by exceeding the solubility limits of inclusion forming reactants in the liquid or can be introduced by external contamination events (exogenous). The most common source of nonmetallic inclusions is from melt reactions with dissolved oxygen. Typically, for steel castings, porosity is considered highly detrimental and the most common method to eliminate gas (CO) porosity is the use of deoxidizers (usually aluminum or silicon). This is an effective method of deoxidation, but it results in the generation of a large oxide inclusion population. These oxides can be highly problematic for certain steel grades where there are stringent specifications, having negative effects on castability, mechanical properties, and compliance with cleanliness requirements[1-8].

Current theories about the evolution of nonmetallic inclusions normally include the following stages: (i) nucleation, (ii) growth/agglomeration, and (iii) flotation[1-2]. A review of state-of-the-art theories of liquid steel refining in large scale metallurgical ladles was recently published by Zhang and Thomas[1]. Inclusion nucleation requires chemical supersaturation which is affected by the chemical affinity of active elements to non-metal impurities (S, O, N) in solution in the melt, as well as alloy composition, temperature, and other factors[1]. Nucleation is understood to be the superposition of surface energy increase and bulk free energy decrease. Above some critical radius a stable nucleus is successfully formed and subsequently grows, spontaneously occurring when the critical radii of the nuclei are exceeded. Inclusion nucleation requires chemical supersaturation which is affected by alloy composition, additions, temperature, and other factors[1].

After nucleation, growth of a nonmetallic inclusion occurs through a variety of mechanisms, with the key phenomenon being Ostwald ripening driven by diffusion of elements and local thermodynamics. Growth by agglomeration has also been considered. For sub-micron particles the contacting mechanism for agglomeration is currently thought to be the result of Brownian collision. Somewhat larger particles however, are more affected by melt flow such as turbulent collision or differential flotation velocities according to Stoke's Law[1-2]. This agglomeration process, in the case of Al_2O_3, is more

efficient when the inclusions are in the liquid state which is one goal of CaSi modification treatments. The calcium in this case leads to the formation of a $CaO \cdot Al_2O_3$ liquid state inclusion that is both spherical and has increased tendency to agglomerate, increasing flotation velocity[1-4].

Flotation is best described by Stokes' Law for unstirred systems with low Reynolds numbers where the velocity of a particle is dependent on the density differential and its size according to Equation 1:

$$v_s = \frac{2(\rho_p - \rho_f)}{9\mu} g R^2 \qquad (1)$$

where: v_s is the particle velocity, ρ_p is the particle density, ρ_f is the fluid density, g is the gravitational constant, and R is the particle radius. Stirring with argon gas is used to aid in inclusion flotation in the ladle. The gas enters through an eccentrically located porous plug in the ladle bottom. The stirring results in reduced content of large sized inclusions. The stirring increases net flotation by both increasing overall fluid velocity, and through inclusion wetting and attachment to the bubble itself, which typically results in reduced content of large sized inclusions[9]. Reynolds numbers for stirred cases are typically invalid for Stokes' Law to be the dominant flotation mechanism, rather than macroscopic flow.

The theories discussed here are well known and supported through countless experiments, but all three basic phenomena (nucleation-growth-flotation) occur simultaneously in liquid steel processing which complicates the study of nonmetallic inclusions[1-2]. It is important to consider that these mechanisms are interrelated and occurring the entire time the steel is in the liquid state. As time progresses the nucleated inclusion populations in the melt are expected to grow in size according to the prevailing growth mechanism, and enlarged particles have increased flotation velocity.

Understanding the overall evolution of inclusions throughout liquid steel refining processes is critical in order to control final product cleanliness[6-7]. Recently, work has been done on the evolution of inclusions in continuous casting steelmaking processes applying an automated SEM-EDS system. This method allows for one to obtain important compositional data with statistical significance when examining such large volumes of production[10-18]. The formation of inclusions in a steel mill can be more

controlled with limited oxygen exposure, narrow ranges of alloying, and consistent product geometry and size. These restrictions are often infeasible for foundries where castings are complex and variable. Work by Singh et al. examined four foundry processes using an automated SEM-EDS system and reviewed the effectiveness of calcium treatments on the inclusion population as well as discussing optimum treatments[13]. In the present study, a similar approach is used to both evaluate the deoxidation practice, the calcium treatment effectiveness in relation to the deoxidation practice, the effect of argon stirring, and to understand the overall evolution of inclusions in the steel foundry processing route for carbon and low alloy steel castings.

Experimental

Industrial Process Sampling

A comprehensive study of steel melt processing at an industrial foundry was performed for three heats (melt through casting). Sampling points for the foundry can be seen in Figure 1 along with an outline of the processing steps at each sampling point, a schematic overview of the process including ladle design, as well as the time at which the samples were taken. The three heats which were sampled include: an aluminum/zirconium deoxidized heat (Heat AA), an aluminum deoxidized heat (Heat B), and an aluminum/zirconium deoxidized heat that employed argon stirring (Heat C). Heats AA and B were not argon stirred. The foundry melts were produced in a 5 ton EAF and poured using a stopper rod bottom-pour ladle. The steel was deoxidized with aluminum or aluminum and zirconium and a calcium treatment was performed using wire injection with steel jacketed CaSi wire. The calcium levels obtained in each heat after the CaSi wire treatment is given in Table 1. The reported final chemistries (via arc spectroscopy) for each heat can is presented in Table 2.

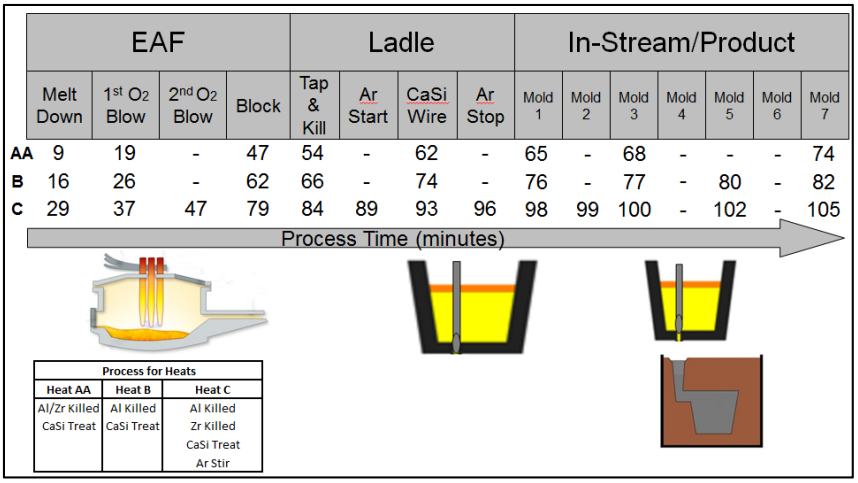

Figure 1. Schematic of three sampled heats (designated AA, B, and C) with process variations and sample locations shown.

Table 1. Calcium content (wt%) after CaSi wire injection.

	Ca (wt%)
Heat AA	0.019
Heat B	0.025
Heat C	0.024

Table 2. Steel chemistry (wt %) measured via arc spectroscopy.

C	Si	Mn	P	Cr	Mo	Ni	Al	Co	Cu	V	Fe
0.25 ± .043	0.52 ± .011	0.80 ± .028	0.025 ± .00005	0.76 ± .040	0.37 ± .011	1.11 ± .037	0.064 ± .013	0.013 ± .00055	0.093 ± .011	0.055 ± .008	bal.

Samples taken in the EAF and ladle prior to casting were unkilled steel chilled immersion samples taken from the top of the melt. The in-stream specimens were acquired from the liquid stream during the casting process (bottom of the ladle). The shape and sectioning method of the samples can be seen in Figure 2. The center sectioning method was used in order to minimize contamination effects, such as scale or slag entrainment that can occur at the surface. Specimens were ground using SiC media (180, 400, 600, 1200 grits), polished using 3µm diamond paste, and finished using a 0.1µm diamond paste. Metallographic preparation was done in accordance to ASTM E3-11 for all samples.

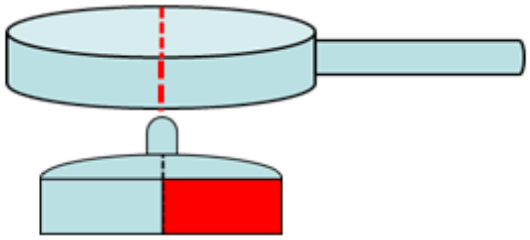

Figure 2. Sample sectioning method used for automated SEM/EDS scans.

Inclusion Analysis

After preparation, samples were scanned using an automated ASPEX SEM/EDS system. Scans were performed using a 0.5µm minimum inclusion diameter threshold (limit of instrument), medium scan speed, 20 keV accelerating voltage, and a nominal EDS detection time of 1 second (Table 3). The step size of the search grid was 0.16µm which allows 100% detection of inclusions as small as 0.5µm in diameter[19]. Porosity was excluded from consideration using an EDS minimum count threshold of 1000, an example of which is shown in Figure 3 where a large region of porosity has been excluded from the analysis due to low counts.

Table 3. ASPEX SEM/EDS settings used in the analysis.

Accelerating Voltage	Emission Current	Nominal EDS Duration	Elements Considered	Exclusion Rules	Mag.	Step Size	Minimum Diameter Threshold	Max Particle Count	Reported Precision
20 keV	40-50 µA	1 second	Mg, Al, Si, Zr, S, Ca, Ti, Mn	> 1000 counts	2000x	0.16 µm	0.5 µm	2500	8%

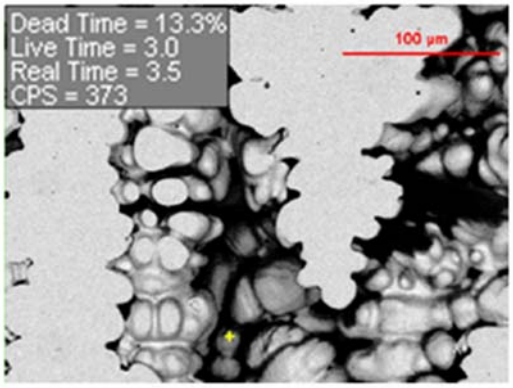

Figure 3. Large region of porosity with low counts per second (CPS) that leads to exclusion from analysis.

Automated analysis provides an averaged EDS spectrum near the inclusion center. In the case of complex or agglomerated inclusion types an additional post-processing filter was applied. The goal of this filtering was de-selection of sulfides from oxides through applying a sulfur concentration threshold (greater than 30% S). The statistical basis of this procedure is given in Harris et al[19]. This technique allows the monitoring of Al_2O_3 modification as well as general oxide modification.

A method of calculating a mass balance from SEM-EDS data was used that allows the study of elemental content contained within inclusions. The areal average elemental composition of inclusions is calculated for each element as follows:

$$\%m = \frac{\sum(\%x)(A_{inclusion})}{A_{total}} \quad (2)$$

where: *%m* is the areal average mass percent of a given element, *%x* is the amount of respective element in an individual inclusion, $A_{inclusion}$ and A_{total} are the area of the individual inclusion and total area of all measured inclusions. The mass balance calculation was performed using the compositional data obtained from the SEM-EDS inclusion analysis and Equation 3:

$$M_{ppm} = \frac{\%m\, A_f\, \rho_i\, w_i}{100\rho_m} \quad (3)$$

where: M_{ppm} is the mass fraction in ppm of a given element in a sample contained within inclusions, *%m* is the areal average mass percent of a given element, A_f is the total inclusion area fraction, ρ_i and ρ_m are the density of the inclusion associated with the given element and the density of the matrix respectively (taken to be iron), and w_i is the mass fraction of the given element in the associated inclusion compound.

Results

The oxide area fraction was examined closely for Heat AA, Heat B, and Heat C and is summarized in Figure 4. The behavior of three size classes of inclusions is shown for each liquid processing stage where these heats were compared for the purpose of determining the effectiveness of argon stirring practice and zirconium additions as a nitrogen/oxygen gettering treatment. A cut-off of 5 μm was arbitrarily used for the "large" size fraction. It was observed that with the addition of zirconium, the total oxide

area fraction of inclusions grows with time in the ladle and that, concurrently, the inclusion size distribution shifts to larger diameters. The opposite is true when only aluminum is used. In this case, the inclusion population shifts from large area fraction with coarse particles to a finer size distribution and a lower area fraction with time in the ladle.

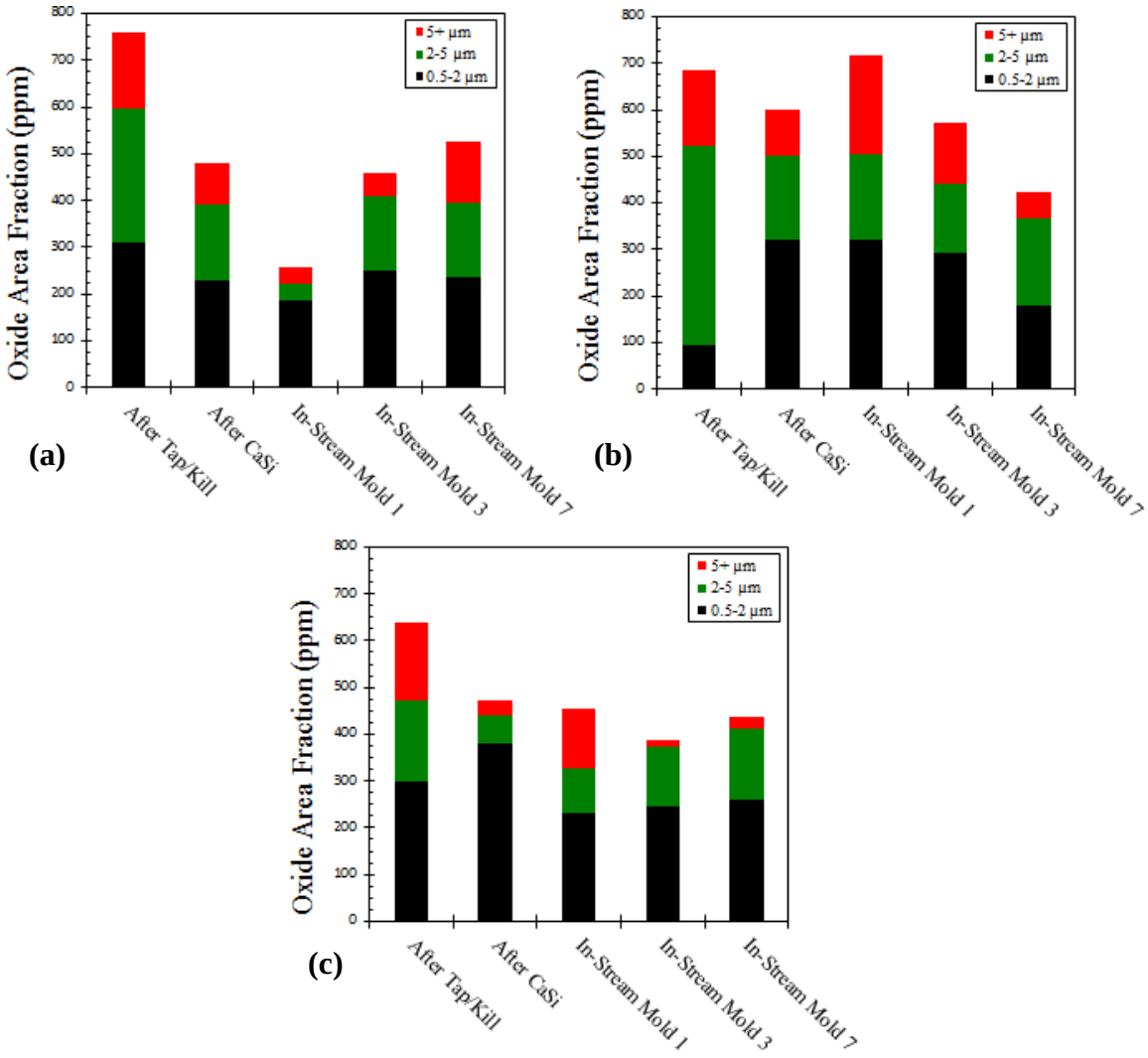

Figure 4. Oxide area fraction for three size ranges across a) Heat AA, b) Heat B, and c) Heat C.

The difference in behavior of the inclusion population with time in Heat AA and Heat B (Figure 5) appears to result from the difference in deoxidation practice used and its effect on inclusion flotation. Each melt was poured into 7 molds of known weight while in-

stream sampling was performed from the pouring stream below the bottom of the ladle. Different molds in the sequence represent different melt levels in the ladle, where the first mold is from the bottom region of the ladle, and the last mold is near the top region. In Heat B (Al killed), the oxide area fraction was found to decrease going from the bottom of the ladle to the top over a time interval of eight minutes. In the case of Heat AA (Al+Zr killed), the opposite was found to be true: the oxide area fraction increased going from the bottom of the melt to the top. The upper quarter of the ladle appeared to accumulate an increased area fraction of inclusions compared to the bottom quarter of the ladle (500 ppm compared to 250 ppm) over a time interval of twelve minutes. By comparison, Heat B showed a drop from 700 ppm to 400 ppm oxide area fraction. Heat C, which was argon stirred, retained a uniform low level of oxide area fraction (450-420 ppm) throughout the ladle.

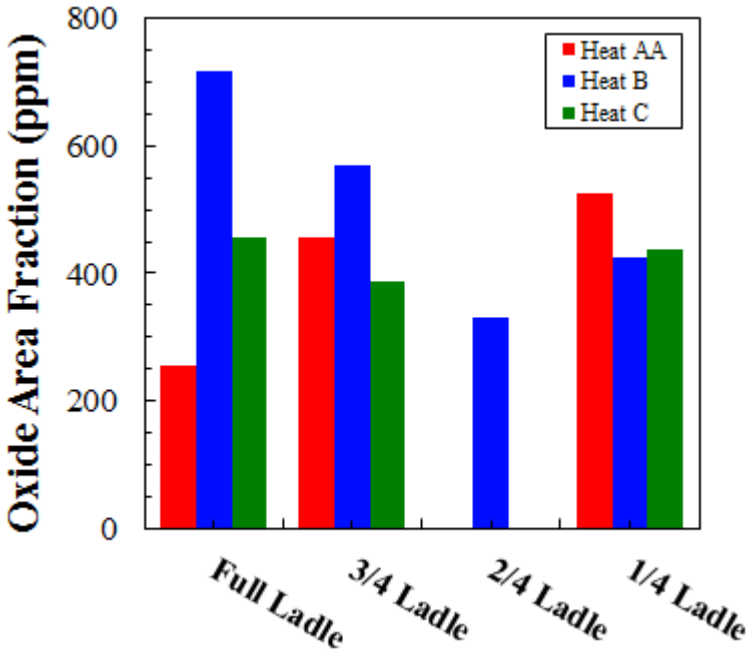

Figure 5. Oxide area fraction as a function of melt level for each heat.

In order to better understand the difference in treatment practice a mass balance calculation based on Eq. 2 was performed for four elements: aluminum, silicon, zirconium, and calcium (Figure 6). It was also found that the content (mass ppm) of aluminum in the samples in the form of inclusions increased immediately after

deoxidation in all heats before decreasing as a result of inclusion removal. The content of silicon in inclusions decreased after deoxidation indicating that the population of silicates was reduced by the more thermodynamically stable Al_2O_3 and/or ZrO_2 according to Eq. 4 and Eq. 5:

$$3SiO_2 + 4[Al] = 2Al_2O_3 + 3[Si] \quad (4)$$

$$[Zr] + SiO_2 = ZrO_2 + [Si] \quad (5)$$

The mass of zirconium reacted to form inclusions increased only after deoxidation in Heat AA and Heat C where zirconium was actually added.

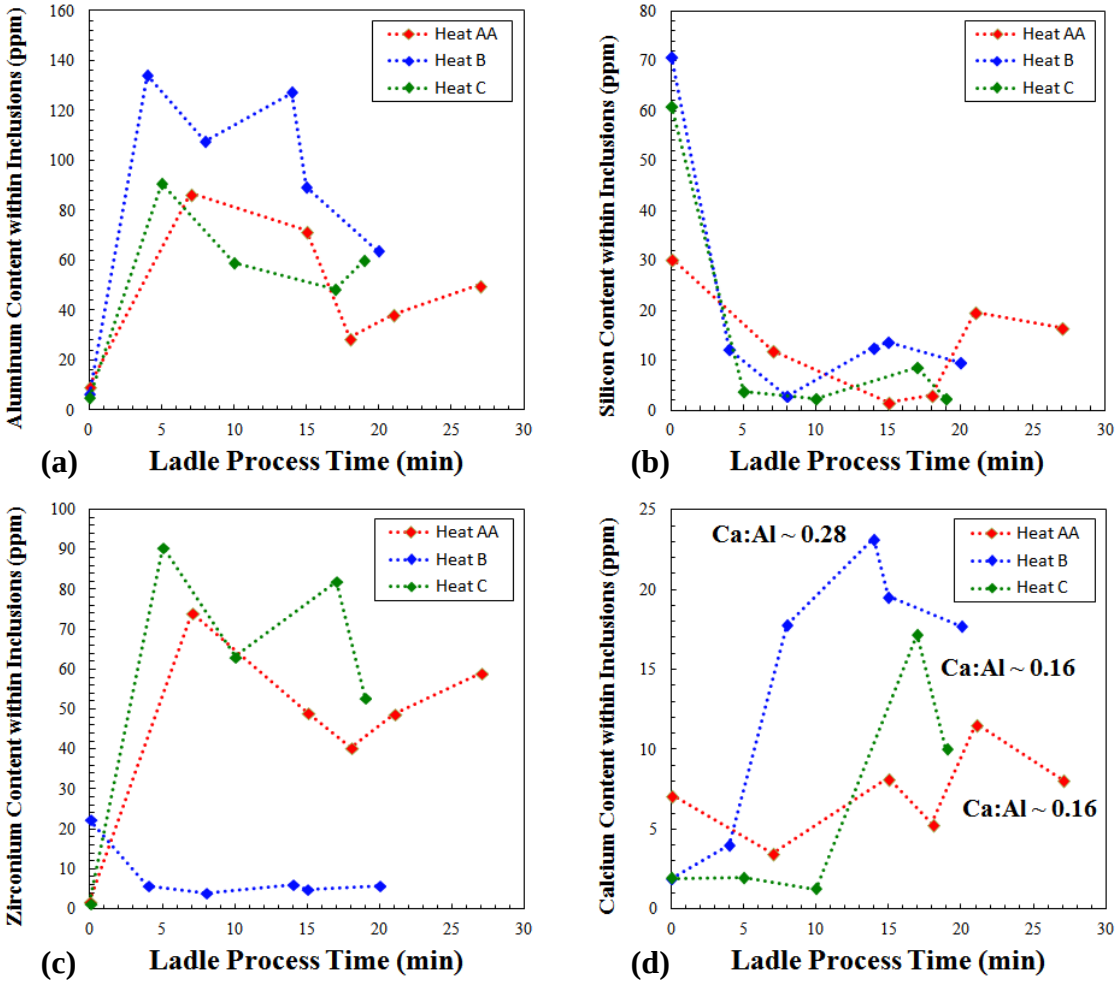

Figure 6. Changing total concentration of active elements within inclusions during ladle processing of analyzed heats: a) Al, b) Si, c) Zr, and d) Ca.

Calcium levels for each heat after CaSi treatment are presented in Table 1. The calcium content of inclusions increased in all heats after the treatment. However, Heat AA retained a lower mass ppm of calcium in the modified inclusions and had a lower final calcium to aluminum ratio (approx. 0.16) than that of Heat B (approx. 0.28). The slag compositions for each sampling are presented in Table 4 and an overview of the composition of the inclusion population (Figure 7) shows the progression of the inclusions for the different deoxidation practices. The composition of the oxide inclusion population after calcium addition for Heat AA can be seen to include a large number of ZrO_2 rich inclusions containing some calcium. In Heat B, very little ZrO_2 is present and most of the population is close to the liquid phase field of the $CaO{\cdot}Al_2O_3$ binary system.

Table 4. Slag chemistries in wt. % of all heats at various liquid process stages.

			%SiO_2	%CaO	%MgO	%Al_2O_3	%TiO_2	%Fe_2O_3	%MnO_2	%ZrO_2	%C
Heat AA	EAF	After Melt Down	50.29	2.91	0.19	8.89	0.39	8.40	29.67	0.82	0.03
		After 1st O2 Blow	50.11	2.14	0.14	7.31	0.34	10.71	28.69	0.60	0.06
		After Block	48.83	2.03	0.16	6.93	0.33	9.30	33.31	0.53	0.17
	Ladle	After Tap/Kill	52.04	1.86	0.18	8.16	0.33	6.81	31.13	0.69	0.00
		After CaSi	49.25	2.13	0.18	9.28	0.36	6.66	32.71	0.86	0.02
Heat B	EAF	After Melt Down	51.72	2.20	0.26	6.27	0.31	18.21	20.13	0.21	0.06
		After Block	52.91	1.43	0.15	5.85	0.34	11.30	28.38	0.16	0.00
	Ladle	After Tap/Kill	51.80	1.41	0.18	8.01	0.34	8.45	30.50	0.18	0.05
		After CaSi	51.48	1.71	0.17	8.92	0.35	7.78	30.47	0.20	0.02
Heat C	EAF	After Melt Down	58.67	3.68	0.17	4.59	0.34	10.67	21.34	0.12	0.03
		After 1st O2 Blow	54.98	3.16	0.21	4.82	0.35	11.73	24.39	0.11	0.03
		After 2nd O2 Blow	54.42	2.69	0.16	4.79	0.33	13.42	23.04	0.11	0.04
		After Block	55.04	2.15	0.18	5.26	0.36	12.34	24.72	0.09	0.03
	Ladle	After Tap/Kill	52.69	2.05	0.19	8.21	0.36	8.73	28.69	0.26	0.06
		After CaSi	52.05	2.34	0.18	8.71	0.38	7.74	28.93	0.61	0.00
		After Ar Stop	52.08	2.30	0.18	8.92	0.38	7.58	29.11	0.59	0.04

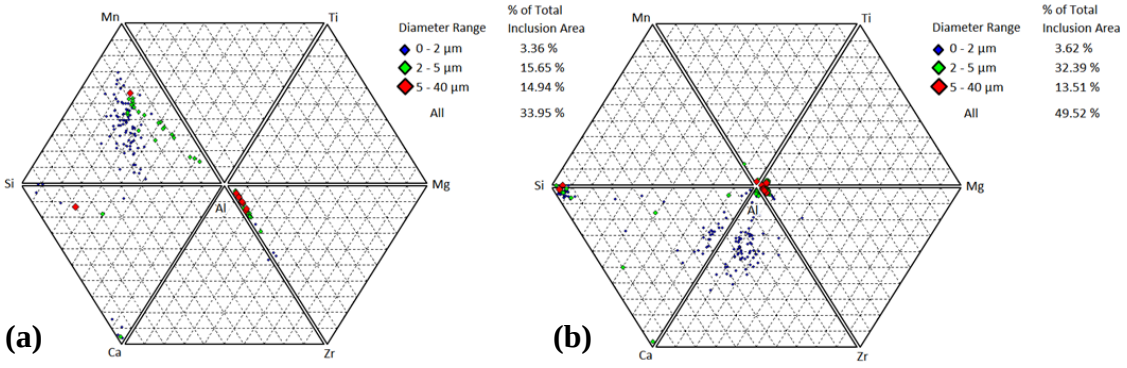

Figure 7. Joint ternary diagrams for a) Heat AA after deoxidation, b) Heat B after deoxidation, c) Heat AA after calcium treatment, d) Heat B after calcium treatment.

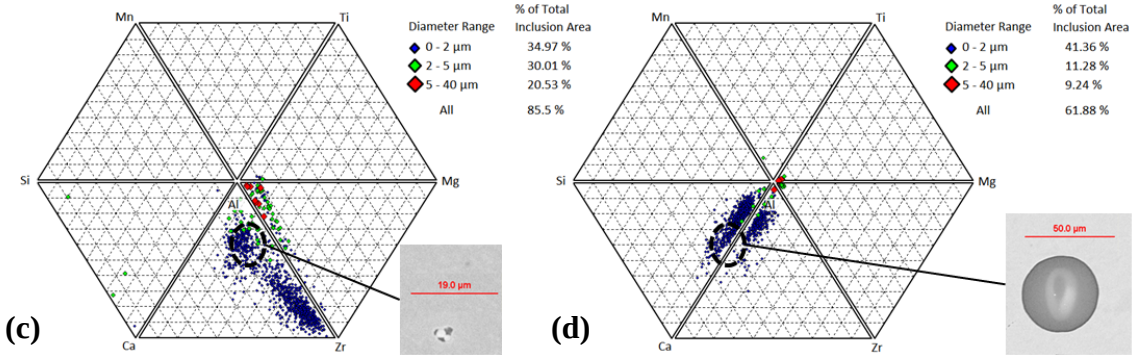

Figure 7. Joint ternary diagrams for a) Heat AA after deoxidation, b) Heat B after deoxidation, c) Heat AA after calcium treatment, d) Heat B after calcium treatment (cont.).

Discussion

Measurements of total oxygen obtained by the inert gas fusion method were compared to calculated mass ppm of oxygen in the oxide inclusions that was obtained from SEM/EDS data. A linear relationship was found (Figure 8), which suggests that most of the oxygen in the steel is present in the form of oxide inclusions. Figure 9, where t=0 is directly after melt down, shows that total oxygen decreases with time after the completion of oxygen blowing in the melt. This indicates that oxygen is being removed from the system. This suggests that the inclusions are being removed by flotation[1-2].

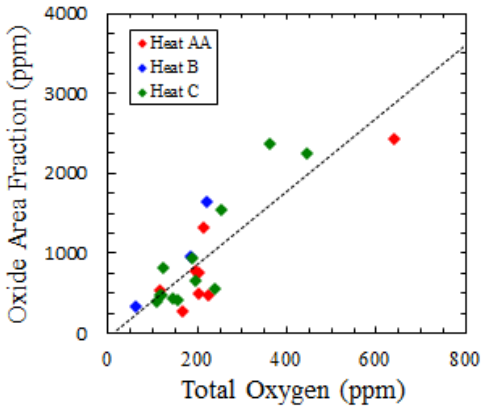

Figure 8. Linear relationship between oxide area fraction and total oxygen measured via inert gas fusion.

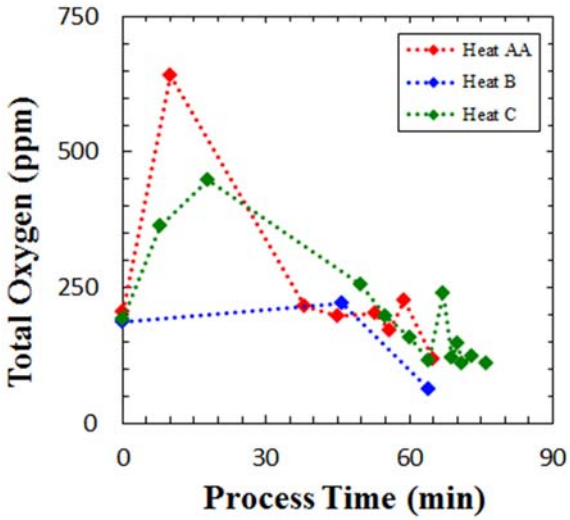

Figure 9. Decreasing total oxygen as a function of liquid processing time for aluminum and aluminum/zirconium treated heats.

The oxide inclusion area fraction decreased with ladle processing time after initial deoxidizing additions, which is also consistent with flotation as the mechanism for oxygen removal (Figure 10). The flotation velocity is well understood from Stoke's Law to be a function of the particle size and density. Thus inclusion growth plays a key role in the removal process. The growth of inclusions can be seen more directly by examining the average inclusion diameter in Figure 11 where the zero time is just before tapping and deoxidation. An initial decrease in size as a result of ladle deoxidation additions that nucleate large populations of small (<2 μm) sized inclusions occurred. A growth period follows where no ladle treatments are made and the melt is held for several minutes.

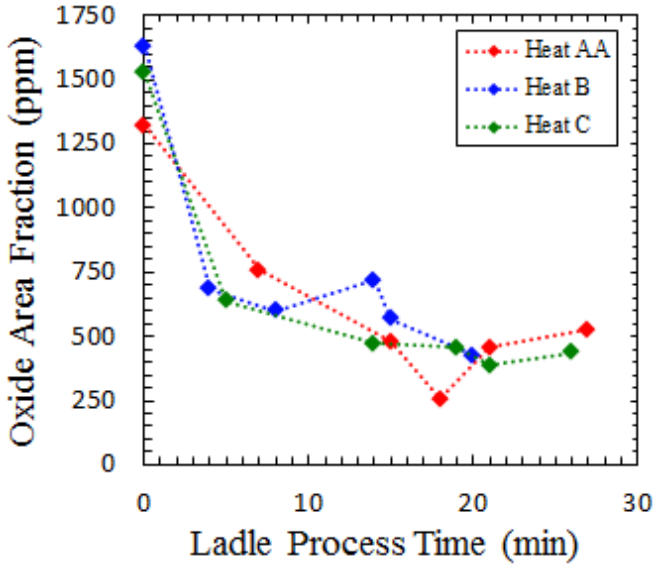

Figure 10. Consistent decrease observed in oxide area fraction with ladle holding time for the heats studied.

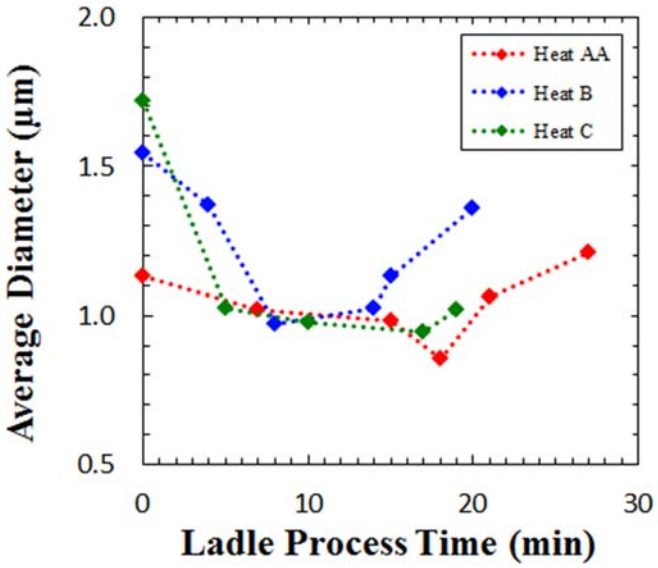

Figure 11. Reduction in inclusion size during deoxidation stages (nucleation) followed by a growth stage.

Deoxidation practice has a large effect on non-metallic inclusion evolution during processing. The composition change of the oxide inclusion population with time in the joint ternary plot (Figure 7) shows the effectiveness of deoxidizing method and modification clearly. The density of the type of oxide formed affects flotation. In the case

of the aluminum deoxidized system, Al_2O_3 was formed which has a density of approximately 4 g/cm³ while the aluminum-zirconium treated heat formed ZrO_2 with a density of approximately 5.7 g/cm³. This density difference leads to a slower flotation rate for ZrO_2 rich inclusions which results in an increase in oxide area fraction at the top region of the ladle when compared to the aluminum killed heat. The Al_2O_3 is more quickly removed from the system as a result of its low density and the effect of calcium treatment aimed at forming liquid $CaO \cdot Al_2O_3$ which speeds flotation further. This faster removal rate leads to a more homogenous melt and a decrease in oxide area fraction over the time span from treatment through pouring the last production casting from the ladle. The use of argon stirring in the aluminum-zirconium treated heat (Heat C) aided the homogenization of the heat and helped mitigate the build-up of oxides in the top region of the melt by assisting inclusion flotation. It is important to note that the addition of zirconium was also expected to act as a nitrogen getter but no ZrN was observed in any samples. This may only be true because of the high oxygen potential of the 7-8% FeO and 29-32% MnO content of the ladle slag (Table 4) that was employed. The nitrogen content for Heat AA was notably high at approximately 500 ppm but still no ZrN formed (Figure 12).

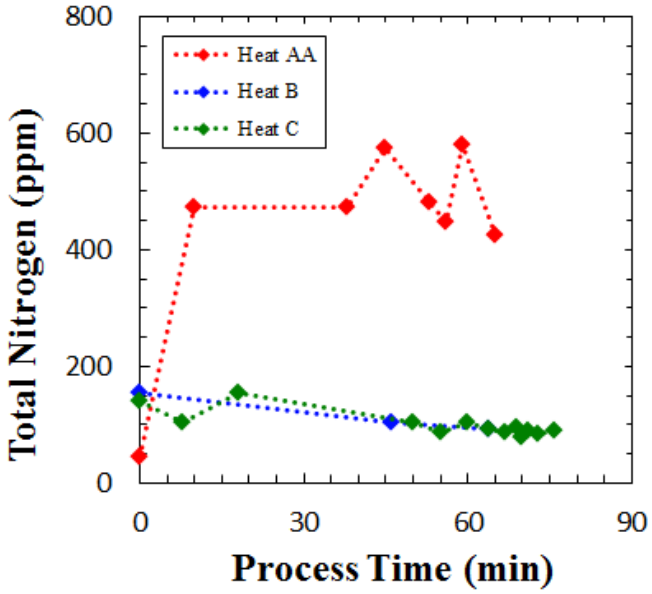

Figure 12. Total nitrogen content measured using inert gas fusion at each sampling point for all heats.

Conclusions

Three industrial 4320 steel heats were followed from melting to ladle pouring in an effort to develop an understanding of the evolution of nonmetallic inclusions through a typical steel foundry process. Immersion sampling was performed at various stages during liquid steel processing in an operating industrial foundry. Three heats with different steelmaking practices were compared: (1) aluminum deoxidized, calcium treated; (2) aluminum/zirconium deoxidized, calcium treated; and (3) aluminum/zirconium deoxidized, calcium treated, argon stirred (Heats AA, B, and C respectively). In order to effectively analyze the evolution of large populations of inclusions, an automated SEM-EDS system was used which enabled a statistically significant number of nonmetallic inclusions to be analyzed.

The aluminum-zirconium treated heats had a lower calcium recovery and exhibited a slower rate of inclusion flotation because of the higher density of ZrO_2 inclusions compared to the Al_2O_3 inclusions generated in an aluminum killed heat. Argon stirring was found to aid in the removal of large sized (> 5μm) inclusions in an aluminum-zirconium treated heat, but had little effect on the inclusion composition. It was noted that using argon stirring in conjunction with an aluminum-zirconium killing practice helped to increase the inclusion flotation rate compared to aluminum-zirconium killing without argon stirring.

References

1. Zhang, Lifeng, and Brian Thomas. "Inclusion Nucleation, Growth, and Mixing During Steel Deoxidation." Continuous Casting Report: 1-19.
2. Deng, Zhiyin, and Miaoyong Zhu. "Evolution Mechanism of Non-metallic Inclusions in Al-Killed Alloyed Steel during Secondary Refining Process." ISIJ International 53: 450-458.
3. Higuchi, Yoshihiko, Mitsuhiro Numata, Shin Fukagawa, and Kaoru Shinme. "Inclusion Modification by Calcium Treatment." ISIJ International 36: 151-154.

4. Yang, Wen, Lifeng Zhang, Xinhua Wang, Ying Ren, Xuefeng Liu, and Qinglin Shan. "Characteristics of Inclusions in Low Carbon Al-Killed Steel during Ladle Furnace Refining and Calcium Treatment." ISIJ International 53: 1401-1410.
5. Van Ende, Marie-Aline, Muxing Guo, Joris Proost, Bart Blanpain, and Patrick Wollants. "Formation and Morphology of Al2O3 Inclusions at the Onset of Liquid Fe Deoxidation by Al Addition." ISIJ International 51: 27-34.
6. Verma, Neerav, Petrus Pistorius, Richard Fruehan, Michael Potter, Minna Lind, and Scott Story. "Transient Inclusion Evolution During Modification of Alumina Inclusions by Calcium in Liquid Steel: Part I. Background, Experimental Techniques, and Analysis Methods." Metallurgical and Materials Transactions B:v42(4): 711-719.
7. Verma, N., Petrus Pistorius, Richard Fruehan, Michael Potter, Minna Lind, and Scott Story. "Transient Inclusion Evolution During Modification of Alumina Inclusions by Calcium in Liquid Steel: Part II. Results and Discussion." Metallurgical and Materials Transactions B: v42(4):720-729.
8. Holappa, L.. "On Physico-Chemical and Technical Limits in Clean Steel Production." Steel Research International 81: 869-874.
9. Lou, Wentao, and Miaoyong Zhu. "Numerical Simulations of Inclusion Behavior in Gas-Stirred Ladles." Metallurgical and Materials Transactions B 44B: 762-782.
10. Singh, Vintee, Kent Peaslee, and Simon Lekakh. "Use of Automated Inclusion Analysis to Evaluate the Effects of Ladle Treatment on Steel Cleanliness."63rd SFSA T&O.
11. Singh, Vintee, Simon Lekakh, and Kent Peaslee. "Using Automated Inclusion Analysis for Casting Process Improvements." 63rd SFSA T&O.
12. Michelic, Susanne, Gerhard Wieser, and Christian Bernhard. "On the Representativeness of Automated SEM/EDS Analyses for Inclusion Characterisation with Special Regard to the Measured Sample Area." ISIJ International 51: 769-775.
13. Singh, Vintee, Simon Lekakh, Timothy Drake, and Kent Peaslee. "Process Design of Inclusion Modification in Cast Steel using Automated Inclusion Analysis."2009. 1-11.

14. Zhang, Zhi, Anders Tilliander, Andrey Karasev, and Par Jonsson. "Simulation of the Steel Sampling Process." ISIJ International 50: 1746-1755.
15. Kawakami, Masahiro, Eiji Nakamura, Shuzou Matsumoto, and Seiji Yokoyama. "Morphological Classification of Inclusions in Steel by Image Processing of Micrograph."ISIJ International 36: 113-116.
16. Abraham, Sunday, Justin Raines, and Rick Bodnar. "Development of an Inclusion Characterization Methodology for Improving Steel Product Cleanliness."2013. 1069-1083.
17. Kaushik, P., H. Pielet, and H. Yin. "Inclusion characterisation – tool for measurement of steel cleanliness and process control: Part 1." Ironmaking and Steelmaking 36: 561-571.
18. Kaushik, P., H. Pielet, and H. Yin. "Inclusion characterisation – tool for measurement of steel cleanliness and process control: Part 2." Ironmaking and Steelmaking 36: 572-582.
19. Harris, Marc, Obinna Adaba, Simon Lekakh, Ron O'Malley, and Von Richards. "Improved Methodology for Automated SEM/EDS Non-Metallic Inclusion Analysis of Mini-Mill and Foundry Steels." AISTech 2015 Proceedings 2015 (2015). Print.

III. Factors Affecting Impact Toughness of Cast Heavy Section 4320 Steel

Marc L. Harris, Von L. Richards, Simon Lekakh, Ronald O'Malley

Metallurgical Engineering
Missouri University of Science and Technology
223 McNutt Hall, 1400 N. Bishop, Rolla, MO 65409-0330, USA
Tel.: 573-341-4717
Email: vonlr@mst.edu

Abstract

An in-mold sampling procedure was developed to procure numerous test samples representative of final heavy section castings in effort to further understand the effect of different metallurgical factors on impact toughness for slow solidification rate high strength cast steel. Samples were tested at -40°C and 25°C to examine how different microstructural features such as nonmetallic inclusions, porosity, and hardness influence the impact energy of the steel for brittle and quasi-ductile fracture modes respectively. SEM fractography was used to characterize failures modes: brittle and quasi-ductile at energies ranging from 14-40 ft-lbs. For brittle fracture, hardness had an adverse influence on impact energy absorbed, while increasing the average area fraction and diameter of nonmetallic inclusions led to slight increases. The opposite trends were observed for quasi-ductile fracture in specimens tested at room temperature. In this case, area fraction of nonmetallic inclusions and porosity decreased the impact energy absorbed.

Introduction

It has been shown by many studies that several microstructural parameters (nonmetallic inclusions, porosity, microstructure and hardness) are critical in terms of mechanical properties, especially impact properties of steel[1-8]. The number density of inclusions, the volume fraction, and the average spacing of the inclusions have all been shown to have strong correlation with impact energy absorbed at room temperature. Increases in volume

fraction and number density have been found to be inversely related to the dynamic fracture toughness and the smaller the inclusion spacing the lower the energy absorbed. Much of this work has been done using CVN impact tests where room temperature (25°C) quasi-ductile fracture is the subject of study; however, the majority of the referred studies were done using specially rolled or cast specimens, such as keel blocks, and did not reflect the properties of the actual heavy section casting.

The use of automated SEM/EDS systems to analyze inclusions is becoming more common for everything from process control to understanding failure mechanisms[1-15]. This is in large part due to the ease of use and large quantities of data obtainable from such an instrument in rather short time. Studies from Peaslee et al. and Bartlett et al. have used these instruments for inclusion analysis in relation to impact properties where they have shown strong correlations exist between parameters such as area fraction and impact energy absorbed[1-2]. The large number of inclusions analyzed in these studies has allowed more repeatable and statistically significant information to be gathered about the behavior of quasi-ductile fracture in the presence of nonmetallic inclusions.

This work will expand the earlier observed relationships considering the effects of different microstructural features in heavy section castings on absorbed impact energy for different fracture modes. Samples were tested at -40°C and 25°C with the goal of linking characteristics of nonmetallic inclusions, porosity, and hardness to impact toughness while keeping the fracture mode consistent for each test temperature. Fracture modes are of course related to the heat treatment process and specifically the microstructure of the steel[3-7]. Effort was done to collect specimens directly in the mold, which represent the real heavy section castings without the necessity of destroying the final product.

Experimental

Samples were taken directly from the molds used to cast heavy section large industrial castings. To collect representative samples without destroying the final casting, sampling was performed using a special hollow core insert (Figure 1) into the no-bake sand mold and connected to the gating system or casting at different heights (Figure 2). MAGMA software was used to simulate solidification in the standalone core insert as well as

together with the whole mold (casting + sampler). The Niyama criterion critical number used for the standalone core insert was 0.7 which is typical for moderately fed heavy section castings (Figure 3). Two 4320 steel heats were investigated: an aluminum killed heat designated as “Heat B” and an aluminum-zirconium killed, argon stirred heat designated as “Heat C,” The base chemistries of the steel were similar (Table 1). Samples collected from both the cope and drag of all the molds sampled were used in this study.

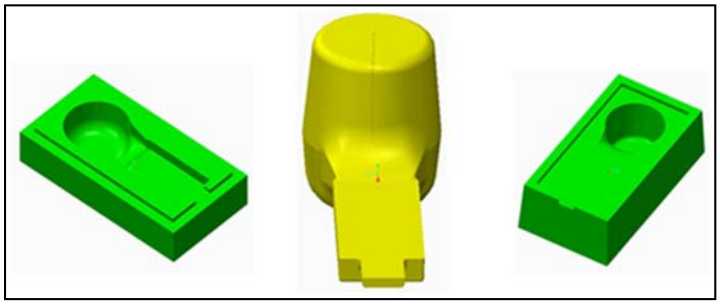

Figure 1. Design of hollow core insert (green) and sampler (yellow)for use inside industrial no-bake sand mold.

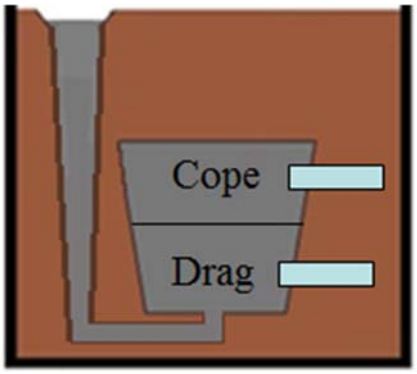

Figure 2. In-mold locations of the hollow core inserts attached to the cope and drag of the casting used to acquire product samples.

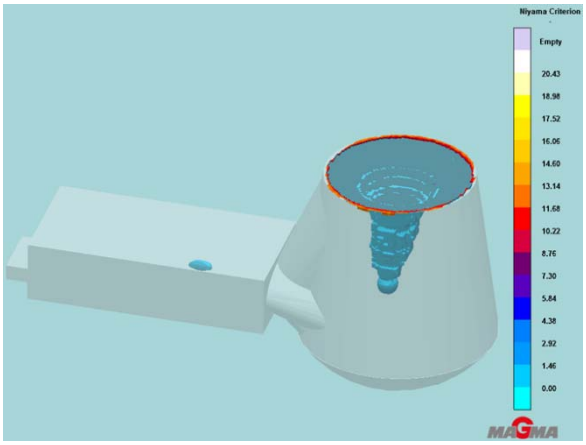

Figure 3. MAGMA solidification model of the standalone sampler with Niyama values below 0.7 highlighted.

Table 1. Steel chemistry (wt %) measured via arc spectroscopy.

	Weight %											
	Fe	**C**	**Si**	**Mn**	**P**	**Cr**	**Mo**	**Ni**	**Al**	**Cu**	**V**	**N**	**S**
Heat B	bal	0.21 ± .02	0.51 ± .004	0.80 ± .02	0.026 ± .0004	0.79 ± .01	0.38 ± .006	1.14 ± .01	0.051 ± .001	0.092 ± .002	0.062 ± .001	0.0093 ± .001	<0.0014
Heat C	bal	0.28 ± .01	0.53 ± .014	0.78 ± .02	0.026 ± .0006	0.73 ± .001	0.37 ± .02	1.11 ± .06	0.074	0.087 ± .005	0.048 ± .0004	0.0088 ± .005	<0.0014

The sampler was used to examine the effect of different features on the impact toughness of the cast steel after heat treatment in accordance with ASTM E-23. A diagram outlining how the samples were sectioned is shown in Figure 4 and all samples were for the analysis. After sectioning, samples were then heat treated following the methods used at the participating foundry which include: hydrogen baking for 15 hours at 232°C, normalization for 1 hour at 926°C, austenitizing for 1 hour at 926°C and quenching in water, and a final temper for 1 hour at 580°C with a water quench. The samples were then machined to within standard and wire EDM was used to notch the specimens.

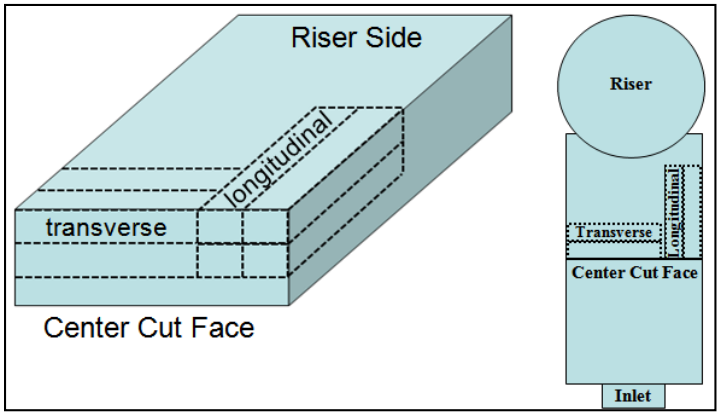

Figure 4. Sectioning method for CVN samples taken from corebox sampler.

Samples were tested on a U-type pendulum impact tester with a non-instrumented hammer at -40°C and 25°C. Each specimen orientation was tested four times to provide a standard deviation and this repeated for every core insert in each heat. The fracture surfaces were examined and four hardness measurements taken for each tested specimen. Samples with brittle fracture having impact energies below 20 ft-lbs were excluded from analysis in the 25°C test where only quasi-ductile fracture modes were being examined. Likewise, brittle fracture mode specimens tested at -40°C with impact energies above 30 ft-lbs were also excluded. This was done to study the effect of microstructural features on impact energy at specific fracture modes. After these selection criteria, the specimens were then sectioned just beneath the fracture surface, polished, and automated SEM/EDS analysis performed on that surface (Figure 5).

Automated SEM/EDS scans were performed using a 0.5µm minimum inclusion diameter threshold (limit of instrument), medium scan speed, 20 keV accelerating voltage, and a nominal EDS detection time of 1 second (Table 2). The step size of the search grid was 0.16µm which allows 100% detection of inclusions as small as 0.5µm in diameter[8].

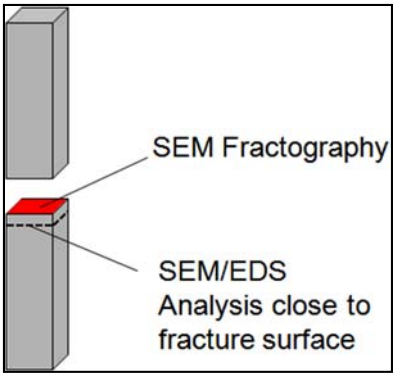

Figure 5. Location of surface used for measuring inclusion content after CVN tests.

Table 2. ASPEX SEM/EDS settings used in the automated analysis.

Accelerating Voltage	Emission Current	Nominal EDS Duration	Elements Considered	Exclusion Rules	Mag.	Step Size	Minimum Diameter Threshold	Max Particle Count	Reported Precision
20 keV	40-50 µA	1 second	Mg, Al, Si, Zr, S, Ca, Ti, Mn	> 1000 counts	2000x	0.16 µm	0.5 µm	2500	8%

Post processing of SEM/EDS data was performed for specific categorization of nonmetallic inclusions and micro porosity with the respective areas, diameters, and coordinates. A method was used to report an average nearest neighboring distance where each center-to-center distance for a nonmetallic inclusion was measured and the minimum value considered a nearest neighbor. This was then repeated for every inclusion in the scanned area and an average reported. A schematic of this process in Figure 6 shows how a single nonmetallic inclusion nearest neighboring distance is measured.

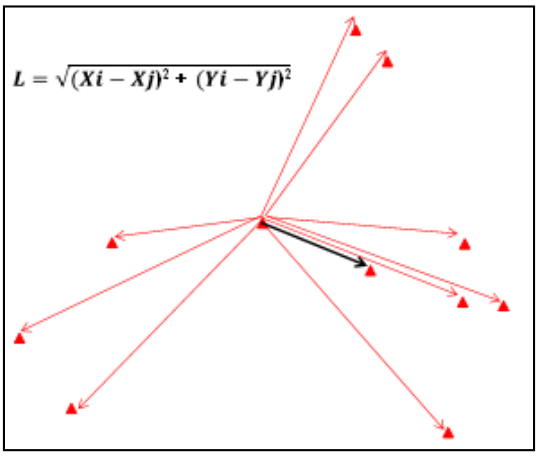

Figure 6. Nearest neighboring distance evaluation technique where the black line denotes the smallest distance.

Results & Discussion

The typical microstructure of a quenched and tempered 4320 steel near the fracture surface contained a lath martensitic structure (Figure 7). However, the similar chemistry and heat treated samples from both heats had a variation in hardness from 33-37 HRC which could be attributed to segregation in the heavy section casting during solidification. Fracture surfaces of -40°C tests showed transgranular cleavage (Figure 8a-8c) as the predominant fracture mode and 25°C tests were dominated by void nucleation (Figure 8d-8e). It is important to note that quasi-ductile fracture surfaces contained regions of nucleated voids, a ductile behavior, while other areas are predominantly transgranular cleavage. The low energy samples have very few regions of ductile fracture whereas at energies between 14-40 ft-lbs the mode can become quasi-ductile with both regions of cleavage and void nucleation. At approximately 50 ft-lbs the entire fracture surface would be considered ductile in nature with no discernible regions of cleavage. This was found to be true for both Heat B and Heat C. It is worthy to note that the especially low impact energies at -40°C may be due to the >0.02 phosphorus content in both heats or the relatively high aluminum used for deoxidation.

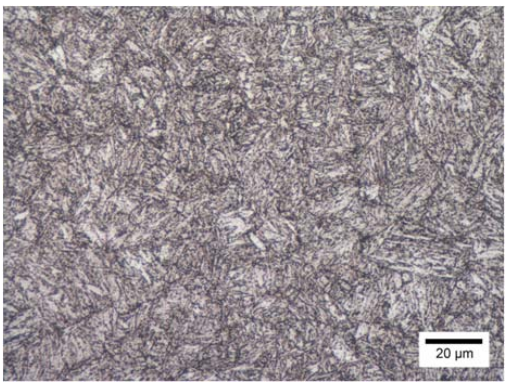

Figure 7. Typical microstructure of CVN sample taken near fracture surface etched with 2% nital for 10s.

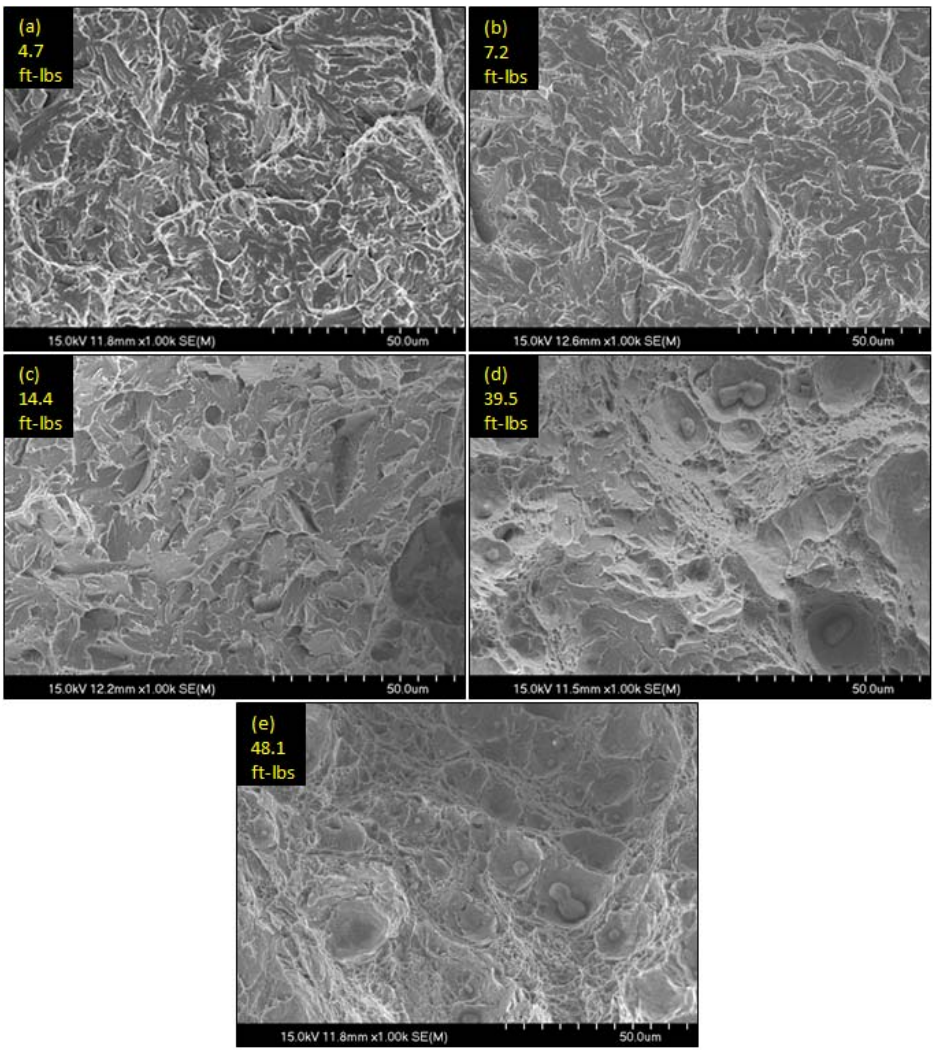

Figure 8. Secondary electron images of CVN fracture surfaces at a) 4.7 ft-lbs, b) 7.2 ft-lbs, c) 14.4 ft-lbs, d) 39.5 ft-lbs, and e) 48.1 ft-lbs.

Table 3 outlines the range of values in impact energies, hardness, area fraction, and average diameter for both heats and testing temperatures. An overview of the nonmetallic inclusion size and chemistry data can be seen in the joint ternaries in Figure 9. Heat B was predominantly $Al_2O_3 \cdot MnS$ complexes, while Heat C contained both $Al_2O_3 \cdot MnS$ complexes and ZrO_2 rich inclusions due to the addition of zirconium during deoxidation.

Table 3. Range of values measured of various microstructural parameters and impact energy absorbed for each heat at each testing temperature.

		HRC	Inclusion Area Fraction (ppm)	Pore Area Fraction (ppm)	Inclusion Diameter (µm)	Impact Energy Absorbed (ft-lbs)
-40°C	Heat B	33.8 - 36.6	670 - 1763	114 - 705	1.6 - 2.2	3 - 20.3
	Heat C	32.9 - 37	552 - 1686	13 - 400	1.2 - 2.1	3 - 20.6
25°C	Heat B	34.8 - 36.6	595 - 1418	76 - 1119	1.7 - 2.2	11 - 50.9
	Heat C	33.8 - 35.6	477 - 952	121 - 872	1.3 - 1.6	17.1 - 44.7

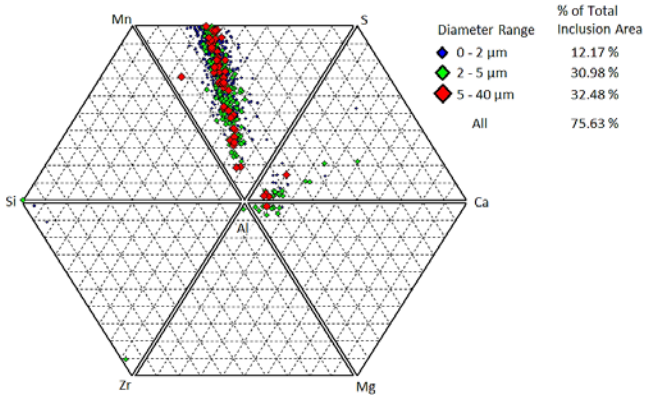

(a)

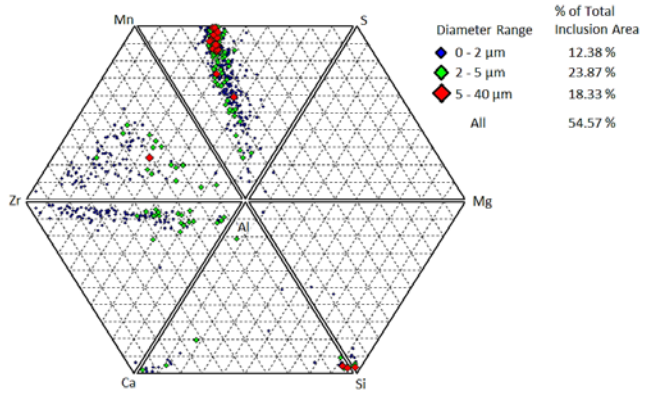

(b)

Figure 9. Size classified joint ternary diagrams for a) Heat B and b) Heat C.

A comparison of impact energy absorbed and the Rockwell C hardness for -40°C specimens shows that increasing hardness greatly reduces the impact energy absorbed for brittle fracture modes in both heats (Figure 10). No such effect was observed for samples tested at 25°C in the quasi-ductile fracture regime for either heat. This could be due to a higher effect of other variables discussed.

The impact energy absorbed depended on the inclusion area fraction in different ways for specimens tested in different fracture modes (Figure 11). An increase in nonmetallic inclusion area fraction led to increased energy absorbed at -40°C, but decreased the energy absorbed at 25°C for both heats. Results for the quasi-ductile fracture mode tests at 25°C agree with what has been reported in literature by Bartlett et al and several others: where increased inclusion content decreased toughness. The brittle fracture mode in the -40°C test results contradict what might be expected from literature maybe since previous tests were typically performed at room temperature[1-5]. It is possible that when the material is already in a transgranular brittle fracture mode, that second phase particles actually impede crack motion through deflection, slightly improving toughness.

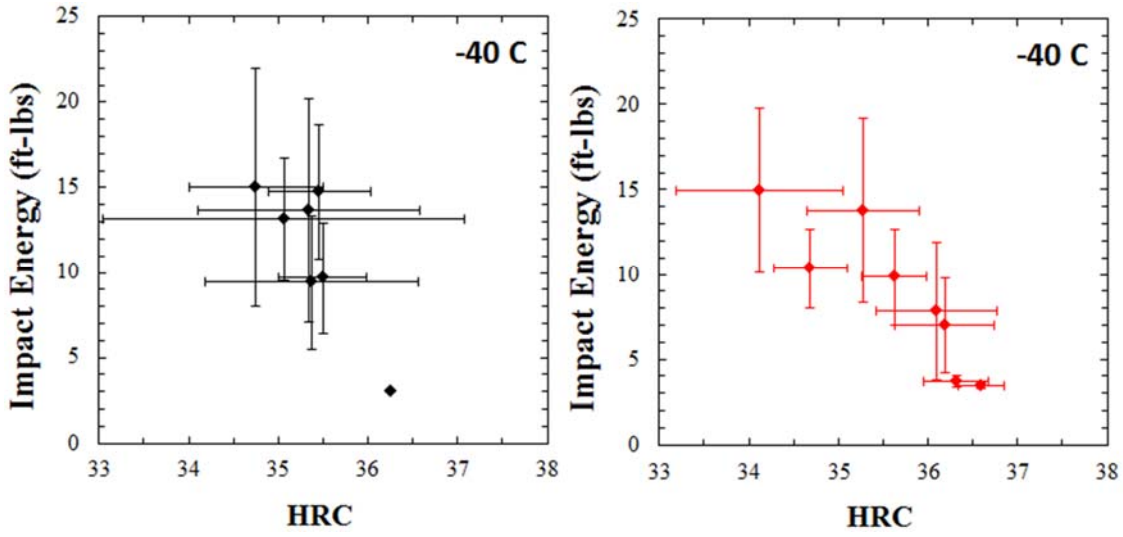

(a) **(b)**

Figure 10. Average impact energy absorbed compared with average Rockwell C hardness of the samples for a) Heat B and b) Heat C.

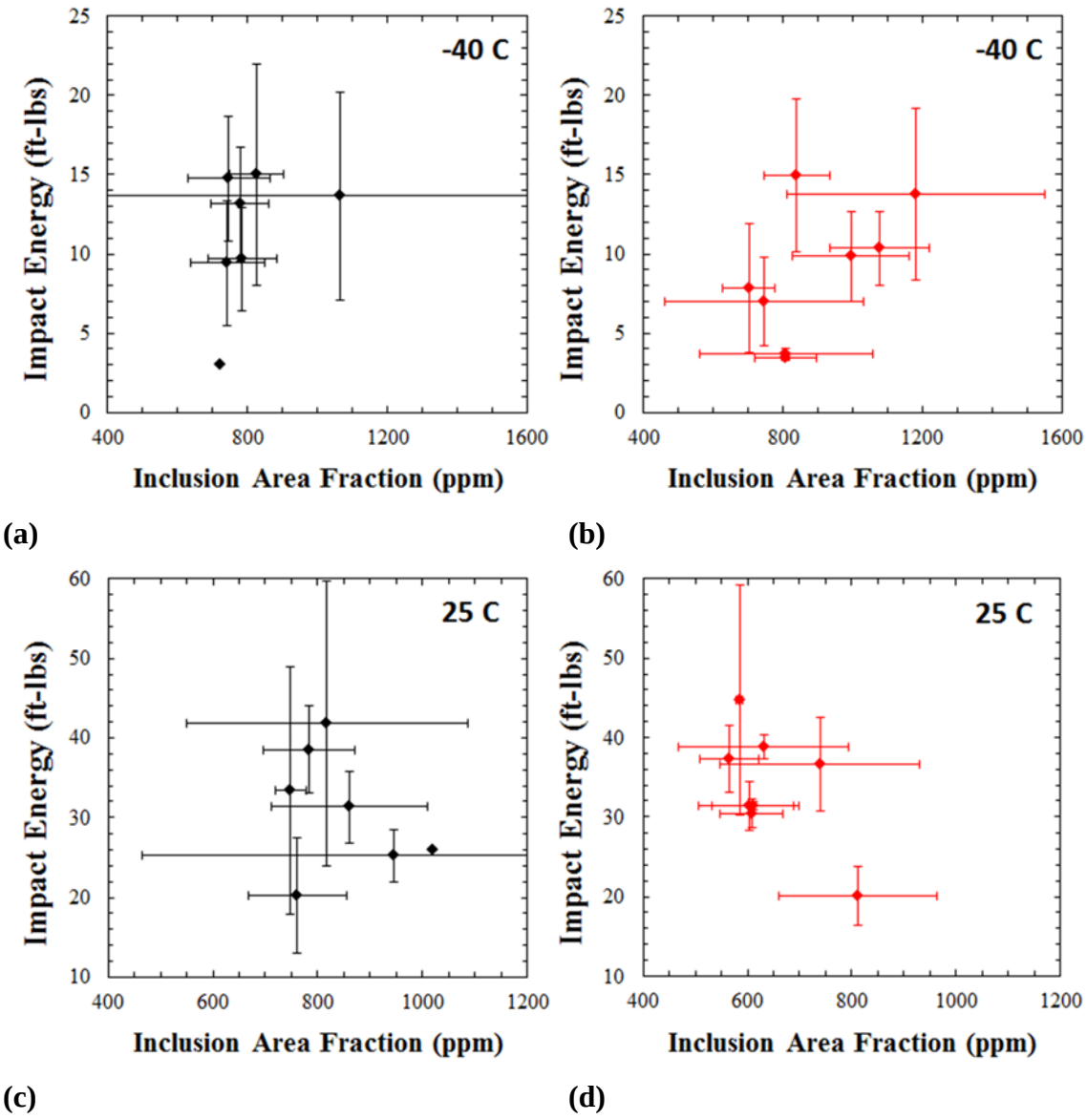

Figure 11. Effect of inclusion area fraction on impact energy absorbed for a) Heat B and b) Heat C at -40°C and c) Heat B and d) Heat C at 25°C.

Inclusion average diameter was plotted against impact energy absorbed in Figure 12a and the toughness was found to increase with inclusion size for brittle -40°C tests. The reverse was noted for ductile 25°C tests in Figure 12b, where increases in inclusion size decreased the toughness.

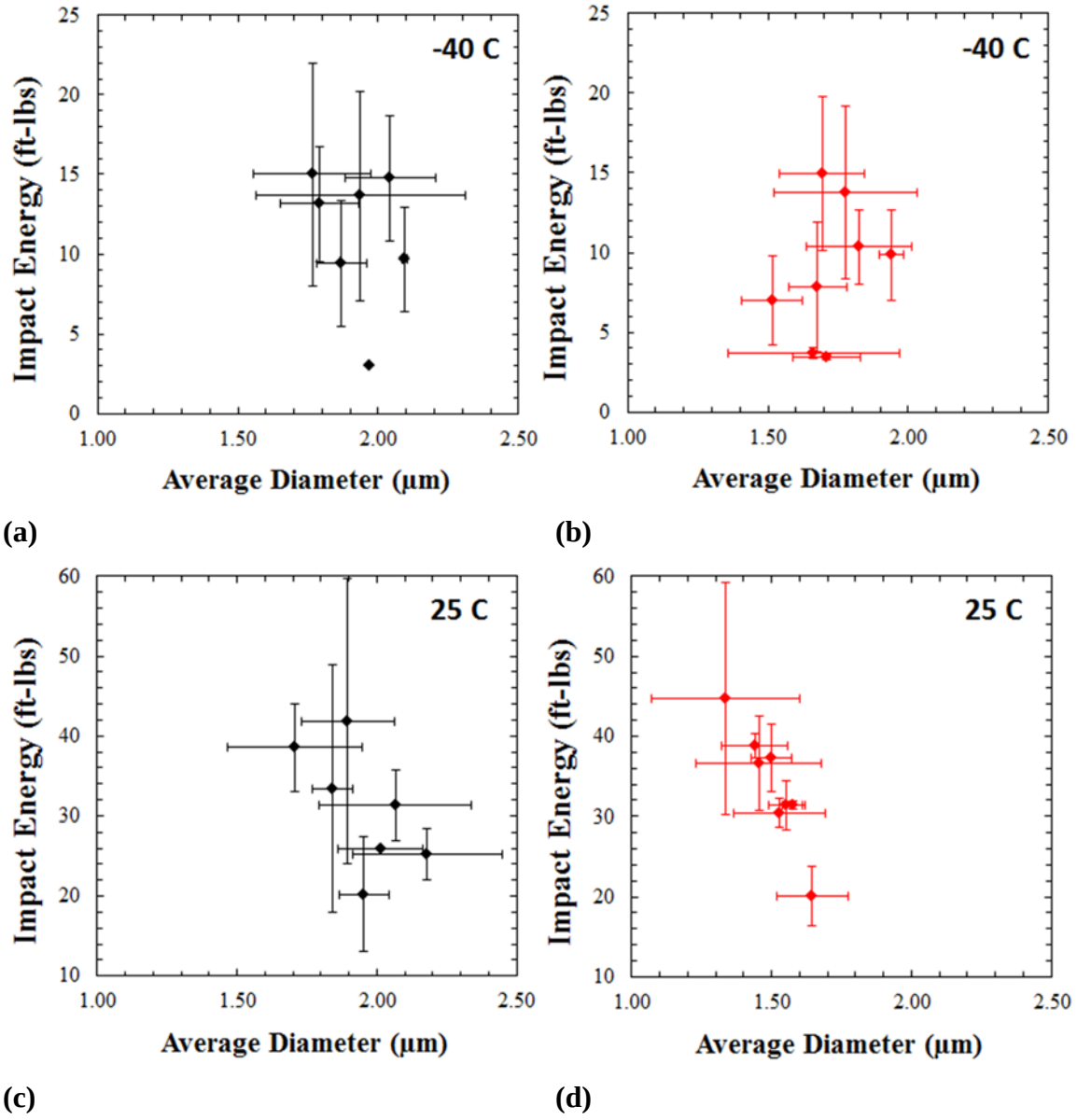

Figure 12. Behavior of impact energy absorbed with average inclusion diameter for a) Heat B and b) Heat C at -40°C and c) Heat B and d) Heat C at 25°C.

It has been shown by a number of studies including Sunday et al. that inclusion spacing plays a large role in fracture, specifically toughness[2,4,8]. Here inclusion spacing was measured directly in the form of nearest neighboring distance and its effect on impact energy absorbed is shown in Figure 13. For both tests, it was found that nearest neighboring distance did not correlate well with impact energy absorbed. This weak

relationship runs counter to previous studies and may be the result of other factors such as average inclusion diameter or area fraction.

Micro-porosity is another important feature for heavy section castings and is often highly unpredictable, seldom considered in addition to other microstructural imperfections. In this study an EDS count threshold of 1000 was applied in post processing of the automated SEM/EDS data to distinguish between nonmetallic inclusions and micro-porosity. In heavy section castings, the variance in porosity can be a detrimental source of error when trying to examine effects of nonmetallic inclusions on impact energy absorbed. The effect of porosity area fraction on impact energy for the quasi-ductile fracture mode 25°C tests can be seen in Figure 14. Naturally the presence of porosity convolutes the study of how inclusions affect toughness. In this case an increasing porosity area fraction ranging from 200-600 ppm reduced the impact energy.

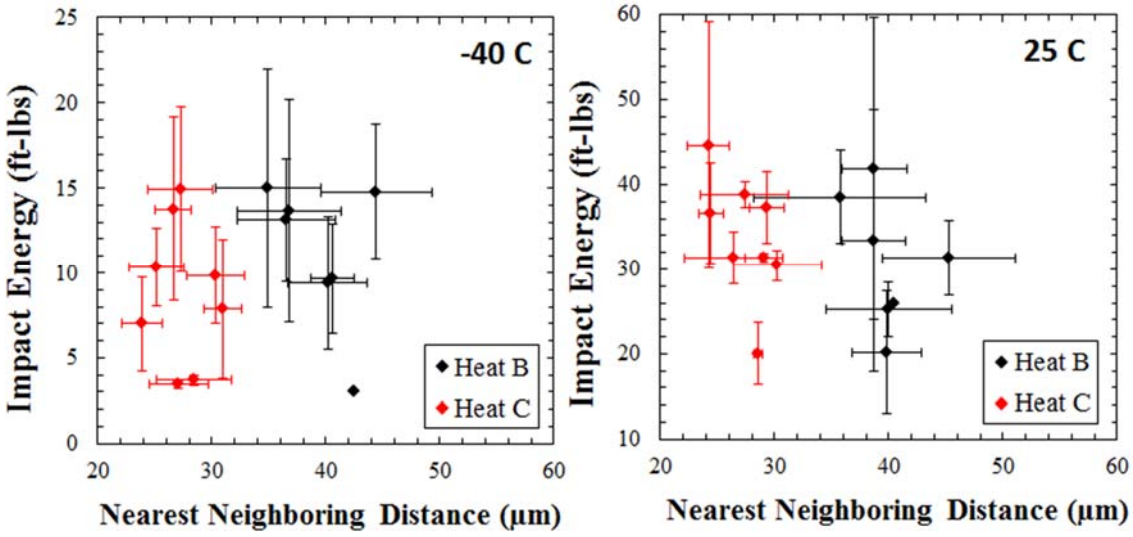

(a) **(b)**

Figure 13. Average inclusion nearest neighboring distance measured with automated SEM/EDS analysis near CVN fracture surfaces for a) -40°C tests and b) 25°C tests.

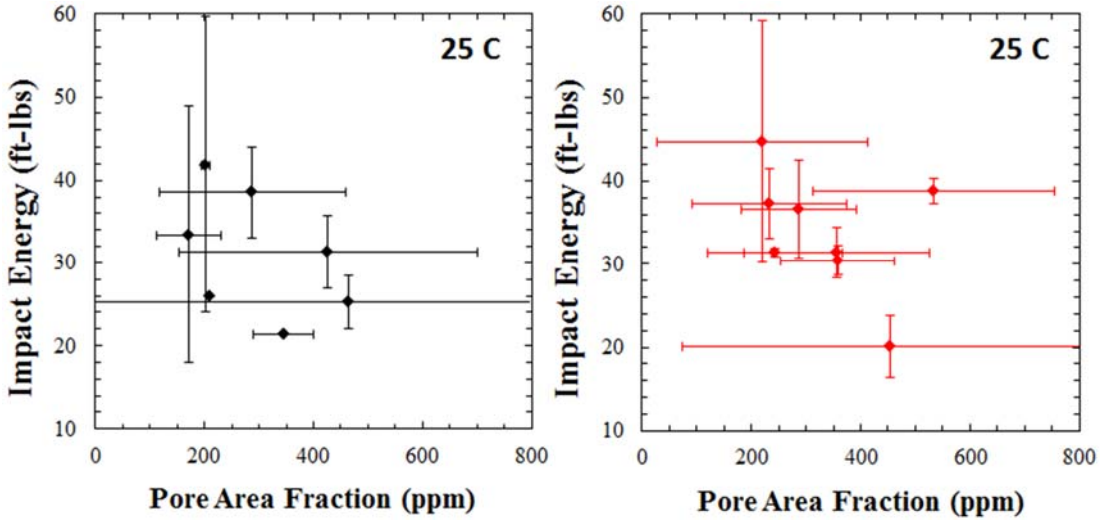

(a) **(b)**

Figure 14. Porosity area fraction effect on impact energy absorbed at 25°C for a) Heat B and b) Heat C.

The addition of porosity and inclusion area fraction into a "defect" area fraction was found to reveal that for aluminum killed steels an increase in defect area fraction greatly increases impact energy absorbed at -40 C (Figure 15) when the fracture mode is transgranular. Conversely, for aluminum-zirconium killed steels increasing the defect area fraction reduces the toughness (Figure 16) when the fracture is quasi-ductile.

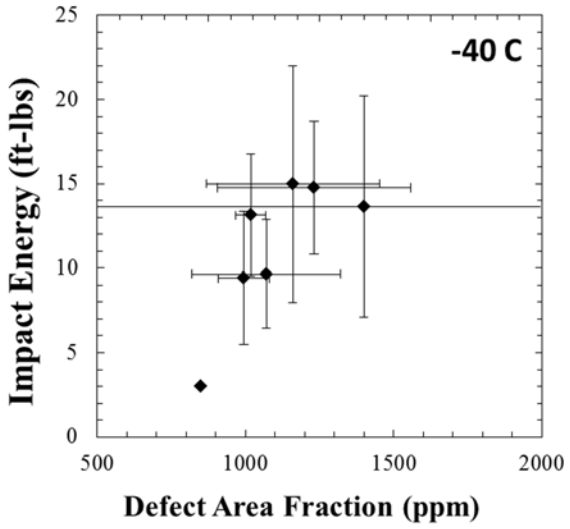

Figure 15. Linear relationship between defect area fraction and impact energy absorbed for Heat B at -40 C.

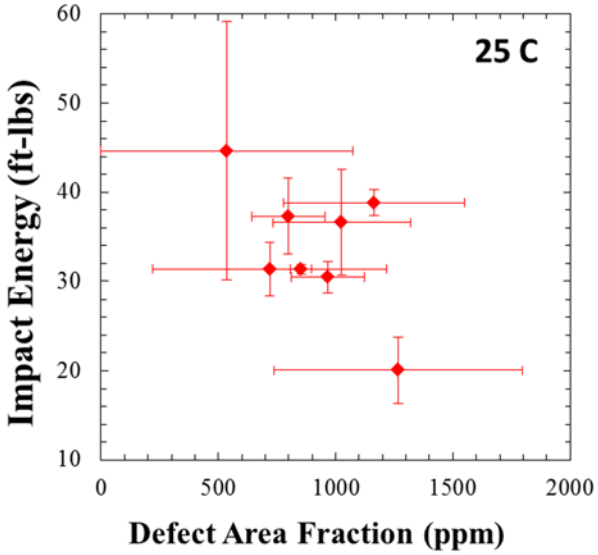

Figure 16. Effect of defect area fraction on impact energy absorbed for Heat C at 25 C.

Conclusions

An in-mold sampling procedure was developed that allowed the collection of large numbers of samples that were truly representative of the final heavy section castings in effort to further understand effects of different factors on impact toughness for low solidification rate high strength cast steel. Samples were tested at -40°C and 25°C to examine how these metallurgical factors influence the impact energy of steel at brittle and quasi-ductile fracture modes respectively.

The effects of inclusion area fraction, average diameter, and nearest neighboring distance on the impact energy absorbed were studied for different fracture modes. It was found that increasing inclusion area fraction and diameter increased impact energy absorbed for brittle fracture modes, likely due to crack deflection by second phase particles. For quasi-ductile fracture increased area fraction and diameter decreased the impact energy absorbed as reported previously by numerous studies. The nearest neighboring distance of inclusions was expected to have a strong correlation with impact energy from previous research, where larger spacing leads to increased toughness. Here a weak correlation was found when using direct measurement of center-to-center spacings. It was determined that this is likely related to other variables such as average diameter increases in conjunction with larger spacing. It was also found that small increases in hardness led to

much lower impact energy absorbed for the brittle fracture mode, while no such effect was observed for quasi-ductile modes. Micro-porosity was found to be unpredictable and to have detrimental effects on impact energy for quasi-ductile fracture mode 25°C tests.

References

1. Peaslee, Kent, Vintee Singh, and Simon Lekakh. "Inclusion Engineering for Improved Properties in Steel Casting." TMS (2011). Print.
2. Bartlett, L., A. Dash, D. Van Aken, V. Richards, and K. Peaslee. "DYNAMIC FRACTURE TOUGHNESS OF HIGH STRENGTH CAST STEELS." International Journal of Metalcasting 7.4 (2013): 17-33. Print.
3. Li, Jie, Feng Guo, Zhi Li, Jun-Li Wang, and Ming-Gao Yan. "Influence of Sizes of Inclusions and Voids on Fracture Toughness of Ultra-High Strength Steel AerMet100." Journal of Iron and Steel Research, International: 254-58. Print.
4. Garrison, Warren M., and Andrzej L. Wojcieszynski. "A Discussion of the Spacing of Inclusions in the Volume and of the Spacing of Inclusion Nucleated Voids on Fracture Surfaces of Steels." Materials Science and Engineering: A: 52-61. Print.
5. Garrison, Warren M., and Andrzej L. Wojcieszynski. "A Discussion of the Effect of Inclusion Volume Fraction on the Toughness of Steel."Materials Science and Engineering: A: 321-29. Print.
6. Choudhary, Pranay, and Warren M. Garrison. "The Effect of Inclusion Type on the Toughness of 4340 Steel." Materials and Manufacturing Processes (2010): 180-84. Print.
7. Hahn, G. T. "The Influence of Microstructure on Brittle Fracture Toughness." MTA Metallurgical Transactions A: 947-59. Print.
8. Abraham, Sunday, Justin Raines, and Rick Bodnar. "Development of an Inclusion Characterization Methodology for Improving Steel Product Cleanliness."2013. 1069-1083.

9. Harris, Marc, Obinna Adaba, Simon Lekakh, Ron O'Malley, and Von Richards. "Improved Methodology for Automated SEM/EDS Non-Metallic Inclusion Analysis of Mini-Mill and Foundry Steels." AISTech 2015 Proceedings 2015 (2015). Print.
10. Holappa, L.. "On Physico-Chemical and Technical Limits in Clean Steel Production." *Steel Research International* 81: 869-874.
11. Michelic, Susanne, Gerhard Wieser, and Christian Bernhard. "On the Representativeness of Automated SEM/EDS Analyses for Inclusion Characterisation with Special Regard to the Measured Sample Area." *ISIJ International* 51: 769-775.
12. Kawakami, Masahiro, Eiji Nakamura, Shuzou Matsumoto, and Seiji Yokoyama. "Morphological Classification of Inclusions in Steel by Image Processing of Micrograph."*ISIJ International* 36: 113-116.
13. Yang, Wen, Lifeng Zhang, Xinhua Wang, Ying Ren, Xuefeng Liu, and Qinglin Shan. "Characteristics of Inclusions in Low Carbon Al-Killed Steel during Ladle Furnace Refining and Calcium Treatment." *ISIJ International* 53: 1401-1410.
14. Van Ende, Marie-Aline, Muxing Guo, Joris Proost, Bart Blanpain, and Patrick Wollants. "Formation and Morphology of Al2O3 Inclusions at the Onset of Liquid Fe Deoxidation by Al Addition." *ISIJ International* 51: 27-34.
15. Singh, Vintee, Kent Peaslee, and Simon Lekakh. "Use of Automated Inclusion Analysis to Evaluate the Effects of Ladle Treatment on Steel Cleanliness."*63rd SFSA T&O*.

SECTION

2. CONCLUSIONS

The effect of step size and magnification settings on the number density and area fraction of nonmetallic inclusions measured by an automated SEM/EDS system was investigated. Magnification was found to have greater effect on the measured area fraction and diameter while the step size had affected the number of inclusions detected. It was determined that step size must be less than the minimum diameter threshold for successful detection of nonmetallic inclusions. By using optimal settings for these parameters it was found that rapidly cooled samples (near the surface of the immersion sample) resulted in more accurate representations of nonmetallic inclusion populations in liquid steel; however the surface was more likely to be contaminated with entrained slag. Post-processing methods and representation techniques for data acquired from SEM/EDS systems were developed that include: areal average compositions, mass balance calculations, and joint ternaries with color coded size data.

Immersion sampling was performed at every liquid process stage that was feasible in the industrial setting for the participating foundry considered for three heats with varied deoxidation and stirring practice. The zirconium treated heats resulted in less effective calcium treatment and slower flotation as a result of the higher density of ZrO_2 inclusions compared to Al_2O_3. The use of argon stirring aided in the removal of large sized (> 5μm) inclusions with little effect on the overall inclusion chemistry.

Novel in-mold sampling was performed that allowed sample collection truly representative of the final heavy section castings. CVN tests were performed at -40°C and 25°C to examine how metallurgical factors influence the impact energy of steel at brittle and quasi-ductile fracture modes. It was found that increasing inclusion area fraction and diameter increased impact energy absorbed for brittle fracture modes, likely due to crack deflection by second phase particles. Quasi-ductile fracture modes showed the reverse, increased area fraction and diameter decreased the impact energy absorbed which agrees with previous work. The nearest neighboring distance of inclusions was expected to have a strong correlation with impact energy from literature, where larger spacing leads to

increased toughness. A weak correlation was found when using direct measurement of center-to-center spacings where increasing the spacing actually led to reduced impact energy absorbed. It was determined that this is likely related to other variables such as average diameter increases in conjunction with larger spacing. It was also found that small increases in hardness led to much lower impact energy absorbed for brittle fracture, while no such effect was observed for quasi-ductile fracture modes. Micro-porosity was found to be unpredictable and to have detrimental effects on impact energy for quasi-ductile fracture in 25°C tests. It was therefore determined that the sorting micro-porosity from nonmetallic inclusions is critical in determining impact toughness behavior.

APPENDIX A.
DATA EDITOR MODULE

Upon clicking start in the data editor tab of the software the data module menu will open. An image of what the data editor module in the post-processing software can be seen in Figure A.1. The input file field is the file to be analyzed (.csv or .xlsx), while the output file field is user-defined (standard file naming convention) and will be the edited .csv file produced. There are three functionalities of the data editor: filtering by a single user-defined rule, exclusion of particular elements, and combining two data files. The original file (input file) is never altered by this module or any other.

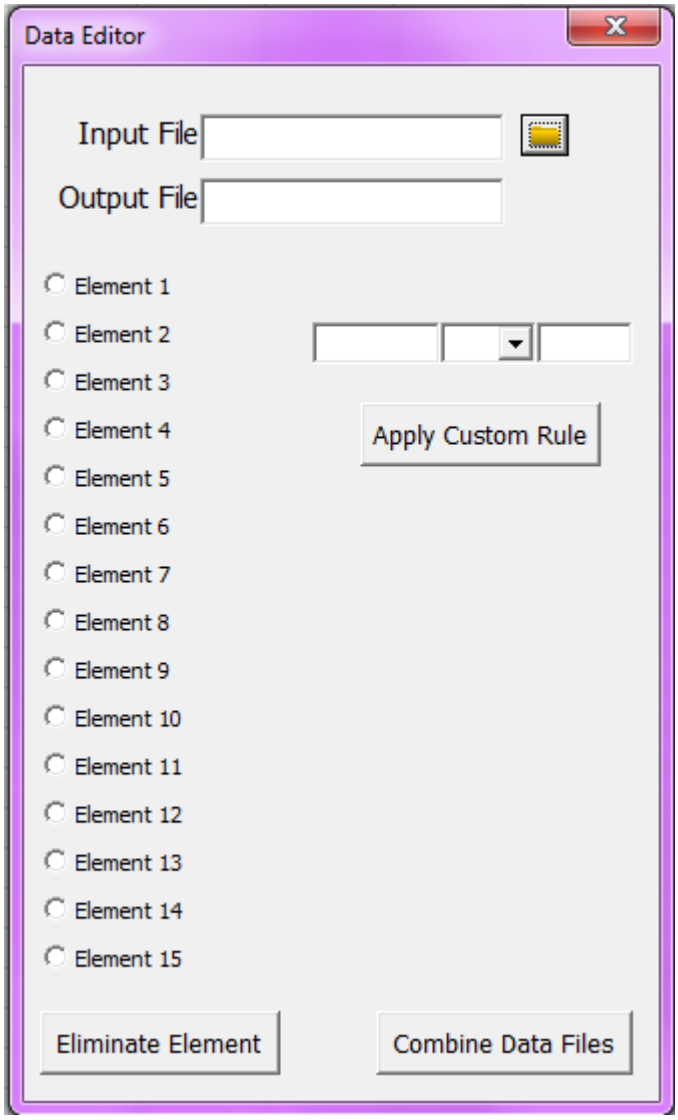

Figure A.1. Data editor module in the SEM/EDS data post-processing software developed.

Applying a custom rule requires an input file, a name for an output file, and inputting the parameter of interest into the left-most text box with the correct character capitalization. The middle text box has a drop down menu containing less than, greater than, and equals to operators. The last text box is the comparator. After these are entered and a name selected for the output file, the program will automatically filter all features in a data file saved as the name input in the output file text box. The location of this file will be in the same folder as the input file.

Eliminating an element requires an input file, a name for an output file, and the selection of 1 element (the list automatically populates). The eliminate element button will then create a file with that element deleted and all other elements normalized to 100%.

Combining data files requires first that an input file be selected, and an output name be chosen before selecting the combine data files button. Upon activation, a file browser will appear where a user-defined .csv or .xlsx file can be selected. After selected a new file with combined data from both will be created.

APPENDIX B.

SEARCHER MODULE & NEAREST NEIGHBORING DISTANCE MODULE

The searcher module is used for getting an overview of the data in terms of population density, area fraction, average diameter, and more. After selecting start, the menu shown in Figure B.1 will appear. The data filename text box is the input data file and the progress.txt file is a file produced by the SEM/EDS software used for the ASPEX Pica 1020. Each of these are selected from a browser after clicking the file box nearby. The progress.txt file step can be skipped and the scan area entered manually into cell A10 under "Scan Area."

After a file is selected, there are 5 possible user-defined filters, with the default being "Part# > 0" which will yield information about every feature in the data file (nonmetallic inclusion or porosity). This can be changed to anything by the user. The left most text boxes are the parameters of interest, the middle text boxes can be "<", ">", or "=," and the last text box is the value being compared against. The software will apply up to 5 user defined filters drawing on the full data if nothing else is selected. This can lead to a feature being displayed for two filters at once (e.g. a single inclusion has both "Part# > 0" and "X_POS < 10" so is displayed for both). The user can then check the "exclusive" box and each filter will be applied in ascending order, removing features that match each criteria from the pool of considered data. If more than one filter is required at the same time, the combine check boxes can be selected in any combination and the fields above and below will be combined (e.g. an inclusion must have "Part# > 0" and "X_POS < 10" for it to be displayed). The critical information text boxes denote what information is to be displayed with the defaults being "X_ABS," "Y_ABS," "AREA," and "DAVE."

After the desired filters are input, the start search button will initiate the searcher function and return the requested information. On the left of the searcher tab a summary table shows general information about the displayed data.

Nearest neighboring distance can be calculated using the "NND" module. After selecting the "NND" tab, the top of the page contains the table and button shown in Figure B.2. Clicking the button will automatically pull the filtered data from the searcher module and calculate the nearest neighboring distance for every feature matching the previously defined criteria (in searcher module). The average nearest neighboring distance will be displayed along with standard deviation and 95% confidence interval

values in the table shown in Figure B.2. This calculation is intensive for both Microsoft Excel and the working memory so it is suggested that all other programs are not running.

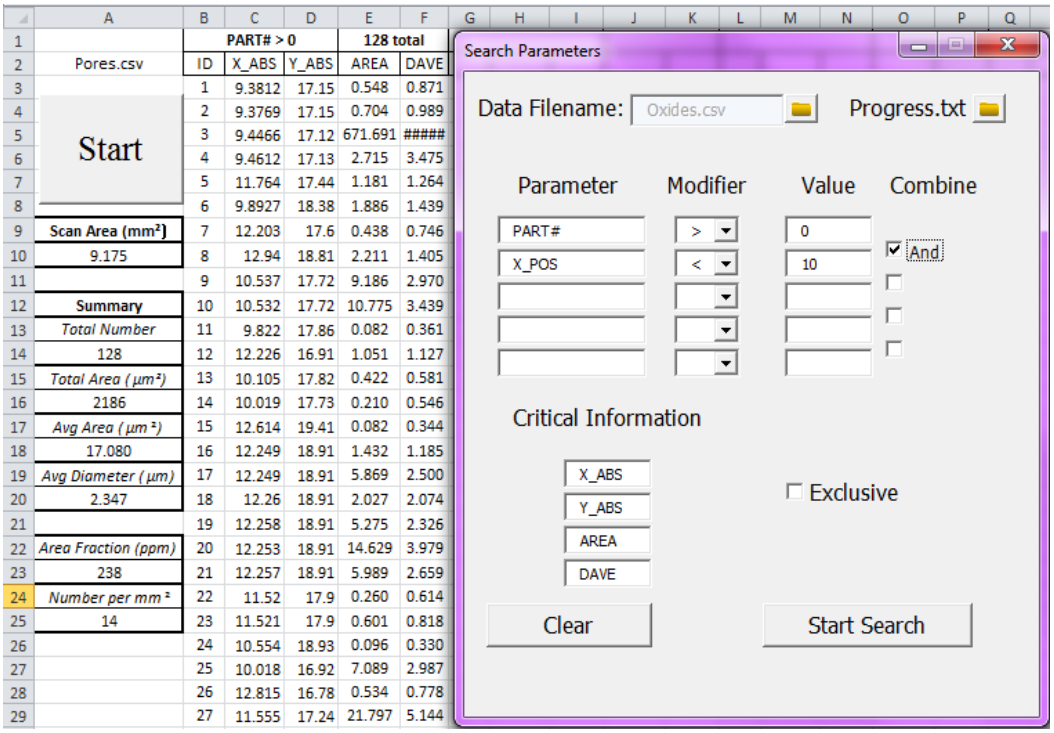

Figure B.1. Post-processing software searcher module menu and output.

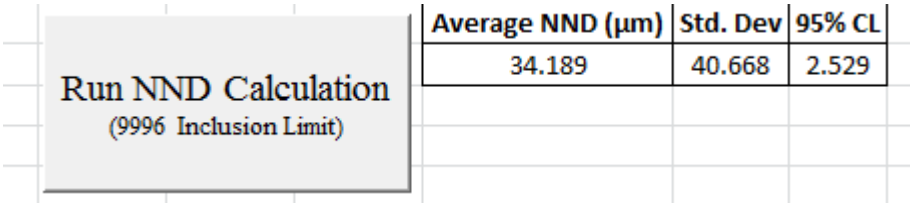

Figure B.2. Nearest neighboring distance module summary table and start button.

APPENDIX C.
AVERAGE CHEMISTRY CALCULATOR

The average chemistry calculator can be activated by going to the average chemistry calculator tab. The starting screen is shown in Figure C.1. Activating the inclusion chemistry importer will bring up the menu shown in Figure C.2. Progress.txt and filename are the same as previously described. Again, the progress.txt can be skipped and the scan area manually input into the scan area cell. A data file must still be opened. Once start is activated the areal average chemistry will be displayed along with the calculated mass of elements within inclusions (displayed as "Total Inclusion Content").

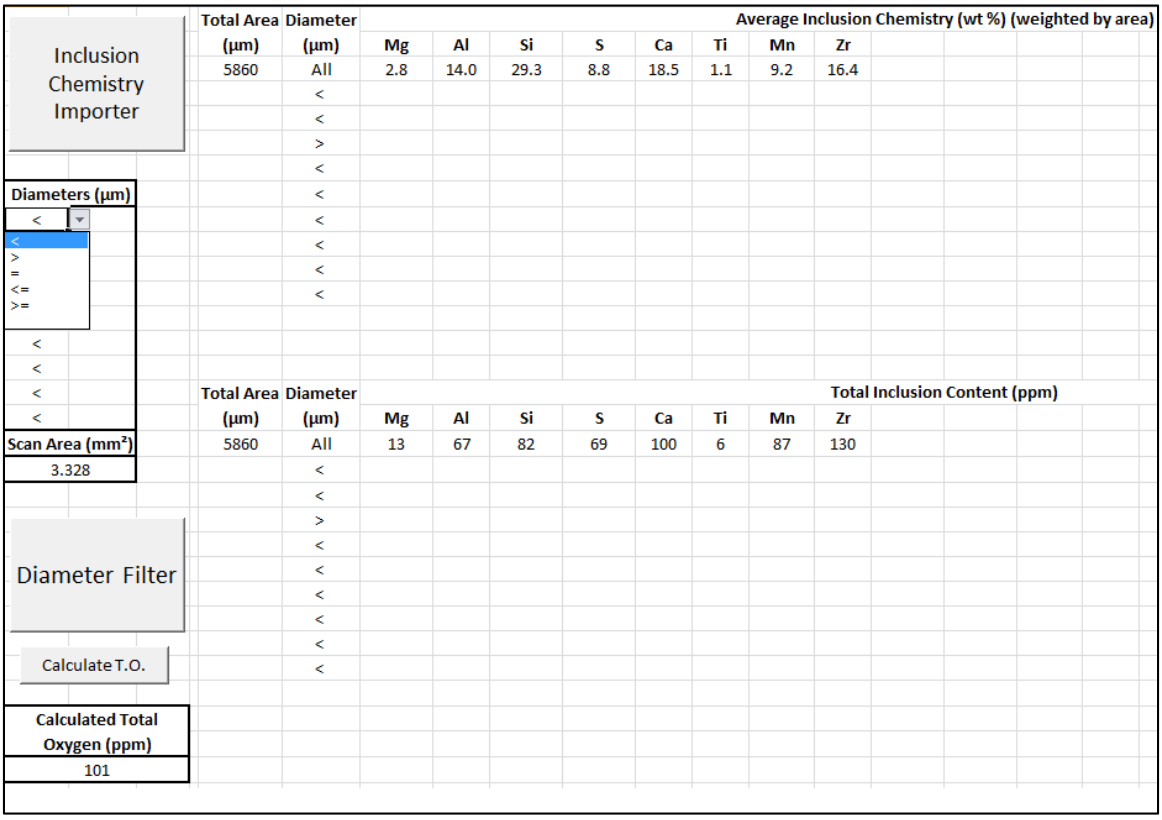

Figure C.1. Overview of the starting screen for the average chemistry calculator module.

The average chemistry and mass balance of elemental content can also be calculated for user defined size ranges by inputting the desired filters into the "Diameters" table shown in Figure C.1. The "Diameter Filter" button will start the process and display chemistries for the input filters. Additionally, the software can approximate the total oxygen in the sample based on the elemental mass balance by selecting the "Calculate T.O." button.

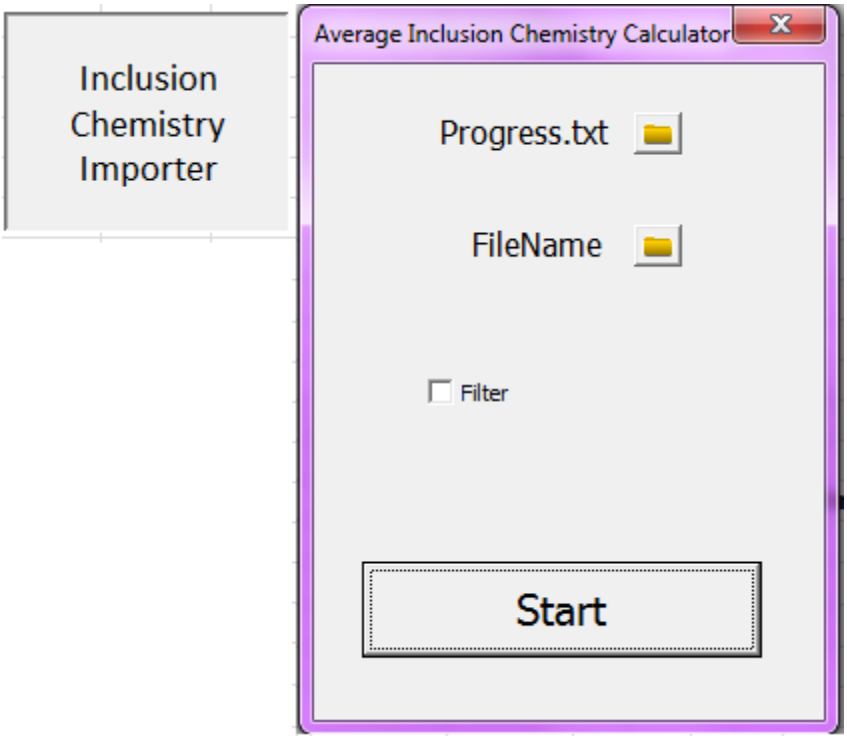

Figure C.2. Inclusion chemistry importer menu next to the button used to activate it.

APPENDIX D.
TERNARY PLOTTER MODULE

The starting screen for the ternary plotter module can be found in Figure D.1. The ternary plotter module will plot each inclusion in a data file in the most representative ternary automatically and show up to 3 user-defined size ranges as different colored and sized points. The file name text box is the input data file to be plotted. A diagram will be shown with the menu that indicates where each user-defined element will appear in the plot. The default elements will be those last plotted while selecting the default button will show an author recommended arrangement. Selecting the "Size Information" checkbox enables size color-coded points on the plot. Once plot is selected the diagram should automatically populate as long as the elements input exist in the data file.

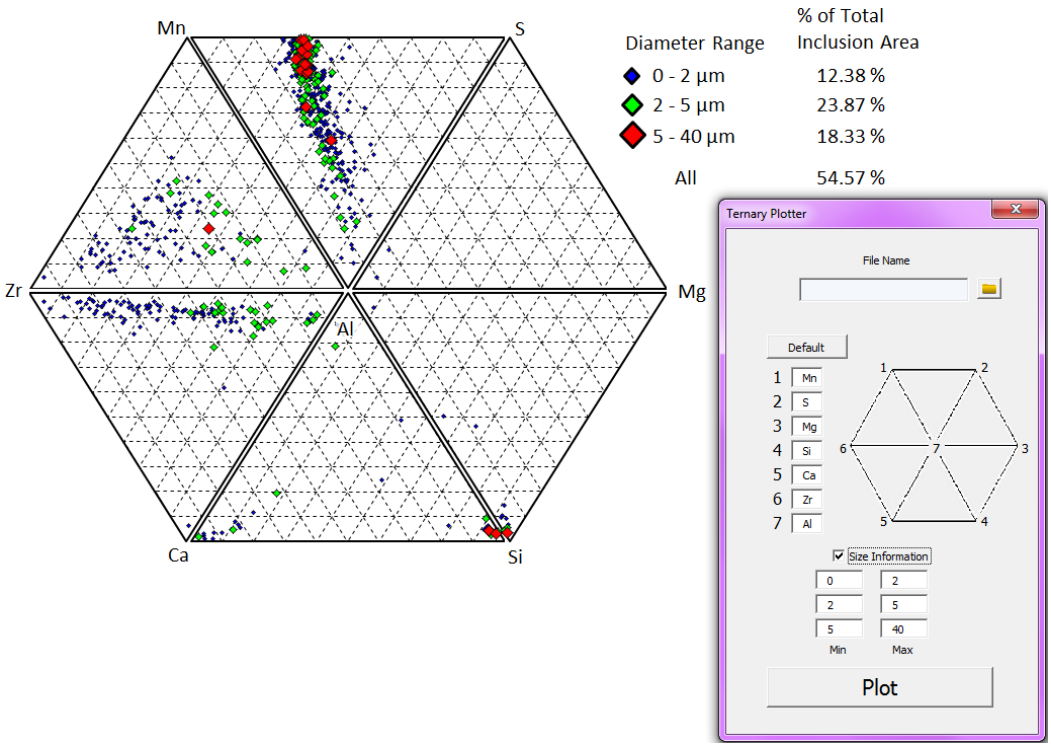

Figure D.1. Data post processing ternary plotter module for generating joint ternary diagrams.

APPENDIX E.
CLUSTER DETECTOR MODULE

If clustered features exist in an analyzed SEM/EDS data file the cluster detector module is ideal for finding and quantitatively measuring them. The cluster detector will automatically detect based on x and y coordinates if a feature is clustered and measure important statistics such as the number of features in a cluster, cluster diameter, area of each cluster, the area fraction occupied by clusters, and more. The criteria used for distinguishing a clustered feature is schematically shown in Figure E.1 where the maximum diameter of each feature is extended along the perimeter and any intersecting feature is considered within range to be a cluster. To use the cluster detector, selecting the "Cluster Detector" button will activate the menu as shown in Figure E.2 where an input data file must be selected. After pressing start the software requires several minutes to complete and will automatically display the results. Once completed, mapping may be performed by selecting the mapping button immediately after the cluster detector has finished. This will display the color coded clustered features with the respective ellipsoidal shapes and orientations. Note that the resulting map may appear difficult to see in the case of large scan areas with very small features.

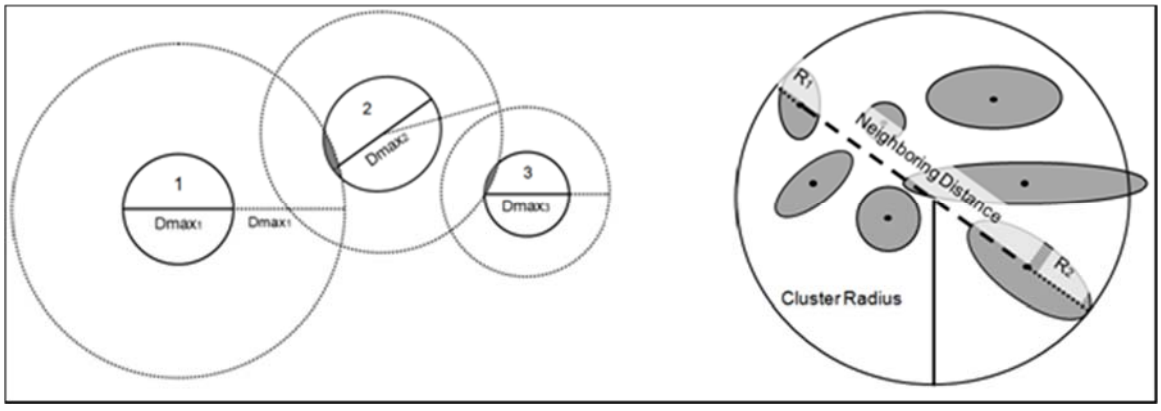

Figure E.1. Criteria used for what is considered a cluster and the method used to measure the effective diameter of a cluster employing maximum neighboring distance within a cluster.

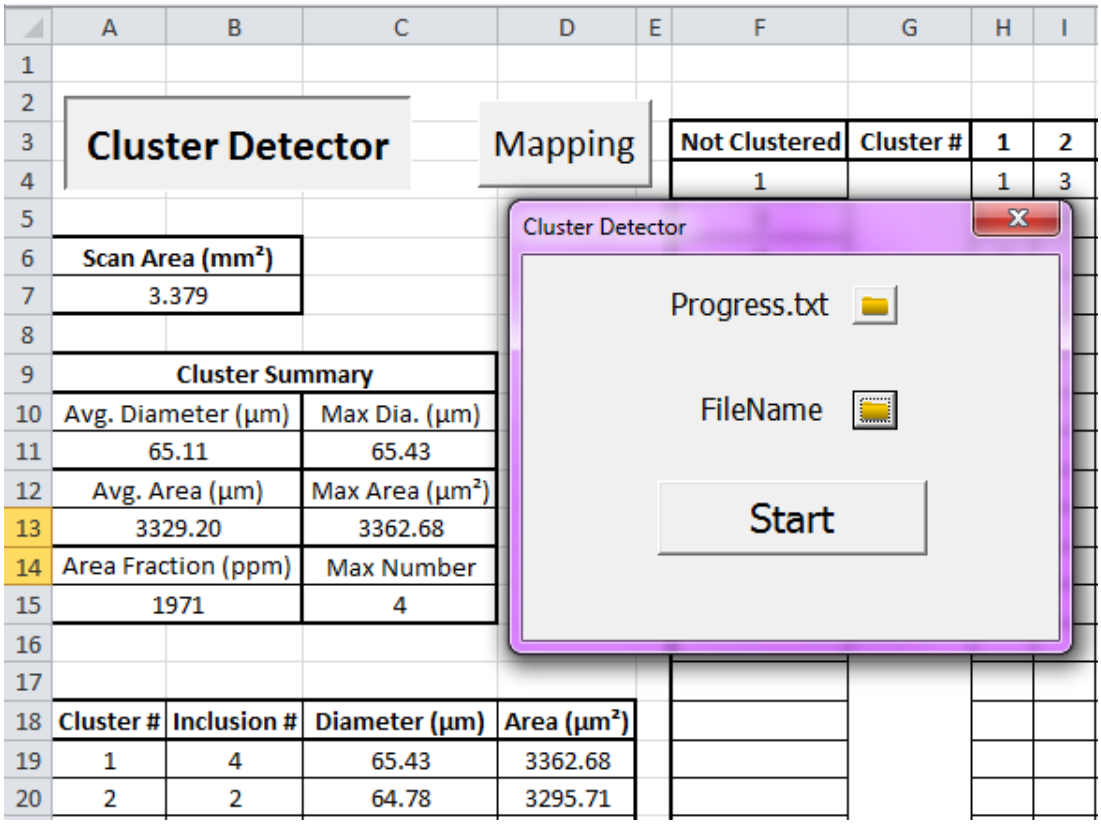

Figure E.1. Starting screen for cluster detector module in the data post-processing software along with output summary table.

APPENDIX F.
IMPACT TEST RESULTS

The results of CVN tests, automated SEM-EDS scans of the sub-fracture surfaces, and hardness are shown in Table F.1.

Table F.1. Raw data from CVN impact tests, SEM-EDS analysis, and hardness testing.

	Heat C 25 C													
	Pore Area Fraction (ppm)		Inclusion Area Fraction (ppm)		# of Inclusions per mm²		Average Nearest Neighboring Distance (µm)		Avg Diameter (µm)		Impact (ft-lbs)		HRC	
	Ind.	Avg	Ind.	Avg	Ind.	Avg	Ind.	Avg	Ind.	Avg	Ind.	Avg	Avg	Big Avg
1st Cope horizontal	382	286.8	827	738.8	208	241.8	23.97	24.4	1.59	1.5	30.8	36.6	34.0	34.3
	147		477		303		23.85		1.12		44.6		34.5	
	362		934		256		23.78		1.59		33.2		-	
	256		717		200		26.13		1.52		37.7		-	
1st Cope vertical	-	219.5	-	585.0	-	248.5	-	24.2	-	1.3	44.6	44.7	35.1	35.0
	318		588		189		25.12		1.47		22.5		34.6	
	121		582		308		23.27		1.20		44.7		35.3	
	-		-		-		-		-		-		-	
1st Drag horizontal	528	356.3	647	603.3	155	170.3	28.99	26.4	1.62	1.6	31.0	31.4	35.0	34.9
	254		505		157		28.17		1.52		35.3		35.6	
	-		-		-		-		-		27.9		34.1	
	287		658		199		22.07		1.52		30.2		34.9	
1st Drag vertical	442	533.8	560	631.0	195	210.5	25.96	27.4	1.44	1.4	36.8	38.8	35.5	34.9
	872		881		282		24.82		1.43		39.5		34.4	
	388		551		140		33.19		1.59		37.8		35.1	
	433		532		225		25.47		1.30		40.2		34.8	
Last Cope horizontal	306	243.5	571	610.5	150	153.5	28.19	29.1	1.56	1.6	31.1	31.4	34.8	34.8
	181		650		157		29.91		1.59		31.6		34.9	
	-		-		-		-		-		-		-	
	-		-		-		-		-		-		-	
Last Cope vertical	445	233.3	579	564.8	166	181.8	31.23	29.3	1.53	1.5	37.1	37.3	34.8	34.9
	205		497		157		29.55		1.58		33.0		34.9	
	159		636		201		28.79		1.48		43.3		-	
	124		547		203		27.53		1.40		35.7		35.1	
Last Drag horizontal	177	454.7	685	812.0	172	184.0	28.50	28.5	1.60	1.6	17.1	20.1	-	34.8
	359		799		208		28.21		1.57		23.6		34.8	
	828		952		172		28.87		1.78		19.5		-	

	-		-		-		-		-		-		-	
Last Drag vertical	306	358.7	551	608.0	138	178.0	33.91	30.2	1.67	1.5	28.5	30.5	33.8	34.3
	305		618		219		27.25		1.38		29.4		-	
	465		655		177		29.56		1.53		31.5		34.8	
	-		-		-		-		-		-		-	
	Heat B 25 C													
	Pore Area Fraction (ppm)		**Inclusion Area Fraction (ppm)**		**# of Inclusions per mm²**		**Average Nearest Neighboring Distance (µm)**		**Average Diameter (µm)**		**Impact (ft-lbs)**		**HRC**	
	Ind.	**Avg**	**Ind.**	**Avg**	**Ind.**	**Avg**	**Ind.**	**Avg**	**Ind.**	**Avg**	**Ind.**	**Avg**	**Avg**	**Big Avg**
1st Cope horizontal	-	345.3	-	761.0	-	149.3	-	39.8	-	2.0	23.2	20.2	35.5	35.9
	324		722		127		42.78		2.01		13.3		36.6	
	311		705		156		39.17		1.87		21.4		36.0	
	401		856		165		37.50		1.98		26.0		35.0	
1st Cope vertical	112	288.3	713	783.8	286	209.5	28.78	35.7	1.45	1.7	41.1	38.6	36.3	36.0
	281		913		253		30.57		1.55		45.2		36.1	
	529		769		141		45.70		1.98		33.3		36.0	
	231		740		158		37.82		1.84		34.6		35.6	
1st Drag horizontal	1119	465.0	1418	946.3	191	142.7	34.44	40.0	2.40	2.2	27.8	25.3	35.8	35.9
	200		826		113		43.71		2.21		25.8		35.6	
	76		595		124		41.85		1.93		22.2		36.3	
	-		-		-		-		-		-		-	
1st Drag vertical	209	209.0	1019	1019.0	142	142.0	40.42	40.4	2.09	2.0	25.9	25.9	35.5	35.5
	-		-		-		-		1.94		-		36.3	
	-		-		-		-		-		-		35.4	
	-		-		-		-		-		-			
-	-	-	-	-	-	-	-	-	-	-	-	-	-	-
	-		-		-		-		-		-		-	
	-		-		-		-		-		-		-	
	-		-		-		-		-		-		-	
Last Cope vertical	105	171.8	716	748.5	142	167.8	39.78	38.7	1.93	1.8	37.7	33.4	35.8	35.1
	238		733		148		39.26		1.83		11.0		35.0	
	203		785		220		34.56		1.75		48.1		34.8	
	141		760		161		41.08		1.86		36.7		34.9	
Last Drag horizontal	422	426.3	726	860.0	111	137.0	48.81	45.3	2.18	2.1	30.7	31.3	35.3	35.4
	670		866		170		39.39		1.79		27.8		35.8	
	187		988		130		47.69		2.24		35.5		35.3	
	-		-		-		-		-		-		-	

Last Drag vertical	199	202.5	681	818.0	160	167.5	40.15	38.7	1.81	1.9	32.8	41.9	34.9	35.4
	-		-		-		-		-		37.8		35.8	
	206		955		175		37.23		1.98		50.9		35.5	
	-		-		-		-		-		-		-	
	Heat B -40 C													
	Pore Area Fraction (ppm)		Inclusion Area Fraction (ppm)		# of Inclusions per mm²		Average Nearest Neighboring Distance (µm)		Average Diameter (µm)		Impact (ft-lbs)		HRC	
	Ind.	Avg	Ind.	Avg	Ind.	Avg	Ind.	Avg	Ind.	Avg	Ind.	Avg	Avg	Big Avg
1st Cope horizontal	-	-	-	-	-	-	-	-	-	-	-	-	-	-
	-		-		-		-		-		-		-	
	-		-		-		-		-		-		-	
	-		-		-		-		-		-		-	
1st Cope vertical	156	238.3	893	779.8	256	189.3	31.19	36.5	1.63	1.8	18.6	13.1	33.8	35.1
	266		772		149		42.03		1.97		11.1		35.8	
	279		764		176		36.63		1.83		12.1		36.0	
	252		690		176		36.30		1.73		10.7		34.8	
1st Drag horizontal	313	284.7	775	785.3	133	129.7	40.77	40.6	2.09	2.1	7.2	9.7	35.8	35.5
	136		704		120		42.18		2.10		12.8		35.0	
	405		877		136		38.82		2.10		9.0		35.8	
	-		-		-		-		-		-		-	
1st Drag vertical	114	334.0	756	825.7	242	211.3	32.88	34.9	1.62	1.8	18.3	15.0	34.5	34.8
	350		892		241		32.34		1.69		18.9		34.3	
	538		829		151		39.61		1.98		7.9		35.5	
	-		-		-		-		-		-		-	
Last Cope horizontal	128	128.0	721	721.0	130	130.0	42.54	42.5	1.97	2.0	3.0	3.0	36.3	36.3
	-		-		-		-		-		-		-	
	-		-		-		-		-		-		-	
	-		-		-		-		-		-		-	
Last Cope vertical	254	251.5	683	743.0	147	160.3	41.21	40.1	1.84	1.9	9.5	9.4	34.8	35.4
	241		676		128		44.22		1.98		6.2		36.6	
	307		709		145		39.39		1.89		15.1		34.0	
	204		904		221		35.79		1.76		7.0		36.1	
Last Drag horizontal	488	485.0	688	746.3	114	127.3	41.02	44.4	2.09	2.0	11.5	14.8	35.4	35.5
	677		866		126		49.25		2.15		14.4		36.0	
	290		685		142		42.94		1.88		18.4		35.0	
	-		-		-		-		-		-		-	
	140	332.0	670	1067.3	232	192.3	33.41	36.8	1.59	1.9	20.3	13.7	36.3	35.3

Last Drag vertical	705		1763		205		35.74		2.25		11.3		35.6	
	151		769		140		41.25		1.98		9.5		34.1	
	-		-		-		-		-		-		-	

	Heat C -40 C													
	Pore Area Fraction (ppm)		**Inclusion Area Fraction (ppm)**		**# of Inclusions per mm²**		**Average Nearest Neighboring Distance (µm)**		**Average Diameter (µm)**		**Impact (ft-lbs)**		**HRC**	
	Ind.	**Avg**	**Ind.**	**Avg**	**Ind.**	**Avg**	**Ind.**	**Avg**	**Ind.**	**Avg**	**Ind.**	**Avg**	**Avg**	**Big Avg**
1st Cope horizontal		275.4	698	807.1	189	185.7	24.89	27.1	1.58	1.7	3.6	3.4	36.4	36.6
			771		178		25.15		1.66		3.3		36.9	
	400		879		203		27.75		1.72		3.5		36.8	
	151		881		172		30.52		1.87		3.3		36.4	
1st Cope vertical	-	-	613	744.4	174	204.9	24.29	23.9	1.53	1.5	8.5	7.0	36.9	36.2
	-		552		170		25.23		1.49		3.0		36.1	
	-		1178		266		21.26		1.65		9.4		35.5	
	-		635		209		24.64		1.38		7.1		36.3	
1st Drag horizontal	-	129.8	1101	1103.4	147	180.1	28.79	25.8	2.05	1.8	10.4	11.2	34.3	34.7
	56		937		206		24.75		1.59		9.7		34.6	
	203		1272		188		23.76		1.88		13.5		34.6	
	-		-		-		-		-		-		35.3	
1st Drag vertical	57	107.3	837	1180.5	198	211.4	28.58	26.6	1.60	1.8	17.8	13.8	34.4	35.3
	-		959		275		24.88		1.52		17.9		35.4	
	129		1239		176		27.30		1.94		6.3		35.9	
	137		1687		197		25.66		2.06		13.0		35.5	
Last Cope horizontal	99	124.3	1182	808.5	208	207.5	26.01	28.4	1.90	1.7	3.5	3.7	36.6	36.3
	-		747		147		32.11		1.89		3.9		36.1	
	138		621		172		30.40		1.62		4.1		36.6	
	136		683		303		25.10		1.24		3.4		35.9	
Last Cope vertical	26	43.3	619	701.9	201	178.8	29.64	30.9	1.56	1.7	12.5	7.9	35.5	36.1
	-		671		168		29.29		1.66		4.7		37.0	
	91		717		161		32.47		1.67		4.1		36.3	
	13		801		185		32.37		1.81		10.2		35.6	
Last Drag horizontal	139	178.3	870	995.5	142	159.5	33.26	30.3	1.98	1.9	9.9	9.9	35.9	35.6
	118		832		151		31.58		1.89		9.9		35.4	
	288		1188		169		28.54		1.97		13.4		35.3	
	168		1092		176		27.83		1.92		6.3		36.0	
Last Drag vertical	154	153.8	979	840.0	199	193.6	23.28	27.2	1.72	1.7	8.7	14.9	35.1	34.1
	-		803		222		27.02		1.58		20.6		34.5	

	-		760		200		28.47		1.56		16.5		32.9						
	-		818		154		30.14		1.90		14.0		34.0						

BIBLIOGRAPHY

[1] Zhang, Lifeng, and Brian Thomas. "State of the Art in the Control of Inclusions during Steel Ingot Casting." *METALLURGICAL AND MATERIALS TRANSACTIONS B* 37B.October (2006): 733-60. Print.

[2] Winkler, W., J. Angeli, and M. Mayr. "Automated SEM-EDX Cleanness Analysis and Its Application in Metallurgy." BHM 152.1 (2007): 4-9. Print.

[3] Kaushik, P., H. Pielet, and H. Yin. "Inclusion Characterisation – Tool for Measurement of Steel Cleanliness and Process Control: Part 1." Ironmaking and Steelmaking 36.8 (2009): 561-71. Print.

[4] Kaushik, P., H. Pielet, and H. Yin. "Inclusion Characterisation – Tool for Measurement of Steel Cleanliness and Process Control: Part 2." Ironmaking and Steelmaking 36.8 (2009): 572-82. Print.

[5] Meyer F Ruby, Evrard S. Vergauwens M., Balland P. “Improvement of the Sampling Methodology for the Cleanliness Measurement in the Liquid Steel Stage.” AISTech 2013 Proceedings (2013): 1051-059. Print

[6] Singh, Vintee, Kent Peaslee, and Simon Lekakh. "Use of Automated Inclusion Analysis to Evaluate the Effects of Ladle Treatment on Steel Cleanliness." 63rd SFSA T&O (2009): 1-15. Print.

[7] Singh, Vintee, Simon Lekakh, Timothy Drake, and Kent Peaslee. "Process Design of Inclusion Modification in Cast Steel Using Automated Inclusion Analysis." AISTech 2009 Proceedings (2009): 1-11. Print.

[8] Shi, Dexiang, and Douglas Winslow. "Accuracy of a Volume Fraction Measurement Using Areal Image Analysis." Journal of Testing and Evaluation (2012): 210-13. Print.

[9] Ericsson, Ola. An Experimental Study of Liquid Steel Sampling. Thesis. Royal Institute of Technology, 2009. Print.

[10] Nuspl, Markus, Wolfhard Wegscheider, Johann Angeli, Wilhelm Posch, and Michael Mayr. "Qualitative and Quantitative Determination of Micro-inclusions by Automated SEM/EDX Analysis." Analytical and Bioanalytical Chemistry 379 (2004): 640-45. Print.

[11] Michelic, Susanne, Gerhard Wieser, and Christian Bernhard. "On the Representativeness of Automated SEM/EDS Analyses for Inclusion Characterisation with Special Regard to the Measured Sample Area." ISIJ International 51.5 (2011): 769-75. Print.

[12] Abraham, Sunday, Justin Raines, and Rick Bodnar. "Development of an Inclusion Characterization Methodology for Improving Steel Product Cleanliness." AISTech 2013 Proceedings (2013): 1069-084. Print.

[13] Zhang, Zhi, Anders Tilliander, Andrey Karasev, and Par Jonsson. "Simulation of the Steel Sampling Process." ISIJ International 50.12 (2010): 1746-755. Print.

[14] Zhang, Lifeng, and Brian Thomas. "Inclusion Nucleation, Growth, and Mixing During Steel Deoxidation." Continuous Casting Report: 1-19.

[15] Deng, Zhiyin, and Miaoyong Zhu. "Evolution Mechanism of Non-metallic Inclusions in Al-Killed Alloyed Steel during Secondary Refining Process." ISIJ International 53: 450-458.

[16] Higuchi, Yoshihiko, Mitsuhiro Numata, Shin Fukagawa, and Kaoru Shinme. "Inclusion Modification by Calcium Treatment." ISIJ International 36: 151-154.

[17] Yang, Wen, Lifeng Zhang, Xinhua Wang, Ying Ren, Xuefeng Liu, and Qinglin Shan. "Characteristics of Inclusions in Low Carbon Al-Killed Steel during Ladle Furnace Refining and Calcium Treatment." ISIJ International 53: 1401-1410.

[18] Van Ende, Marie-Aline, Muxing Guo, Joris Proost, Bart Blanpain, and Patrick Wollants. "Formation and Morphology of Al2O3 Inclusions at the Onset of Liquid Fe Deoxidation by Al Addition." ISIJ International 51: 27-34.

[19] Verma, Neerav, Petrus Pistorius, Richard Fruehan, Michael Potter, Minna Lind, and Scott Story. "Transient Inclusion Evolution During Modification of Alumina Inclusions by Calcium in Liquid Steel: Part I. Background, Experimental Techniques, and Analysis Methods." Metallurgical and Materials Transactions B: n. pag.

[20] Verma, N., Petrus Pistorius, Richard Fruehan, Michael Potter, Minna Lind, and Scott Story. "Transient Inclusion Evolution During Modification of Alumina Inclusions by Calcium in Liquid Steel: Part II. Results and Discussion." Metallurgical and Materials Transactions B: n. pag.

[21] Holappa, L.. "On Physico-Chemical and Technical Limits in Clean Steel Production." Steel Research International 81: 869-874.

[22] Lou, Wentao, and Miaoyong Zhu. "Numerical Simulations of Inclusion Behavior in Gas-Stirred Ladles." Metallurgical and Materials Transactions B 44B: 762-782.

[23] Kawakami, Masahiro, Eiji Nakamura, Shuzou Matsumoto, and Seiji Yokoyama. "Morphological Classification of Inclusions in Steel by Image Processing of Micrograph."ISIJ International 36: 113-116.

[24] Peaslee, Kent, Vintee Singh, and Simon Lekakh. "Inclusion Engineering for Improved Properties in Steel Casting." TMS (2011). Print.

[25] Bartlett, L., A. Dash, D. Van Aken, V. Richards, and K. Peaslee. "DYNAMIC FRACTURE TOUGHNESS OF HIGH STRENGTH CAST STEELS." International Journal of Metalcasting 7.4 (2013): 17-33. Print.

[26] Li, Jie, Feng Guo, Zhi Li, Jun-Li Wang, and Ming-Gao Yan. "Influence of Sizes of Inclusions and Voids on Fracture Toughness of Ultra-High Strength Steel AerMet100." Journal of Iron and Steel Research, International: 254-58. Print.

[27] Garrison, Warren M., and Andrzej L. Wojcieszynski. "A Discussion of the Spacing of Inclusions in the Volume and of the Spacing of Inclusion Nucleated Voids on Fracture Surfaces of Steels." Materials Science and Engineering: A: 52-61. Print.

[28] Garrison, Warren M., and Andrzej L. Wojcieszynski. "A Discussion of the Effect of Inclusion Volume Fraction on the Toughness of Steel."Materials Science and Engineering: A: 321-29. Print.

[29] Choudhary, Pranay, and Warren M. Garrison. "The Effect of Inclusion Type on the Toughness of 4340 Steel." Materials and Manufacturing Processes (2010): 180-84. Print.

[30] Hahn, G. T. "The Influence of Microstructure on Brittle Fracture Toughness." MTA Metallurgical Transactions A: 947-59. Print.

[31] Harris, Marc, Obinna Adaba, Simon Lekakh, Ron O'Malley, and Von Richards. "Improved Methodology for Automated SEM/EDS Non-Metallic Inclusion Analysis of Mini-Mill and Foundry Steels." AISTech 2015 Proceedings 2015 (2015). Print.

VITA

Marc Harris was born in Springfield, MO on December 31, 1988. He received his B.S. in Metallurgical Engineering from Missouri University of Science & Technology in May 2013. He remained at Missouri University of Science & Technology to pursue a M.S. in Metallurgical Engineering under Dr. Von L. Richards through December 2015. In July, 2016 he received his M.S. degree in Metallurgical Engineering from Missouri University of Science & Technology.